

HU ISSN 1586–2070

JOURNAL OF COMPUTATIONAL AND APPLIED MECHANICS

An Open Access International Journal

Published by the University of Miskolc

VOLUME 12, NUMBER 2 (2017)



MISKOLC UNIVERSITY PRESS

HU ISSN 1586–2070

JOURNAL OF COMPUTATIONAL AND APPLIED MECHANICS

An Open Access International Journal

Published by the University of Miskolc

VOLUME 12, NUMBER 2 (2017)



MISKOLC UNIVERSITY PRESS

EDITORS

László **BARANYI**, Institute of Energy Engineering and Chemical Machinery, University of Miskolc, H-3515 MISKOLC, Hungary, e-mail: arambl@uni-miskolc.hu

István **PÁCZELT**, Institute of Applied Mechanics, University of Miskolc, H-3515 MISKOLC, Hungary e-mail: mechpacz@uni-miskolc.hu

György **SZEIDL**, Institute of Applied Mechanics, University of Miskolc, H-3515 MISKOLC, Hungary e-mail: Gyorgy.SZEIDL@uni-miskolc.hu

EDITORIAL BOARD

Edgár **BERTÓTI**, Institute of Applied Mechanics, University of Miskolc, H-3515 MISKOLC, Hungary, e-mail: edgar.bertoti@uni-miskolc.hu

Attila **BAKSA**, Institute of Applied Mechanics, University of Miskolc, H-3515 MISKOLC, Hungary, attila.baksa@uni-miskolc.hu

István **ECSEDI**, Institute of Applied Mechanics, University of Miskolc, H-3515 MISKOLC, Hungary, mechecs@uni-miskolc.hu

Ulrich **GABBERT**, Institut für Mechanik, Otto-von-Guericke-Universität Magdeburg, Universitätsplatz 2, 39106 MAGDEBURG, Germany, ulrich.gabbert@mb.uni-magdeburg.de

Zsolt **GÁSPÁR**, Department of Structural Mechanics, Budapest University of Technology and Economics, Műegyetem rkp. 3, 1111 BUDAPEST, Hungary, gaspar@ep-mech.me.bme.hu

Robert **HABER**, Department of Theoretical and Applied Mechanics, University of Illinois at Urbana-Champaign, 216 Talbot Lab., 104 S. Wright St., URBANA, IL 61801, USA, r-haber@uiuc.edu

Csaba **HŐS**, Department of Hydraulic Machines, Budapest University of Technology and Economics, Műegyetem rkp. 3, 1111 BUDAPEST, Hungary, hoscsaba@vizgep.bme.hu

Károly **JÁRMAI**, Institute of Energy Engineering and Chemical Industry, University of Miskolc, H-3515 MISKOLC, Hungary, altjar@uni-miskolc.hu

László **KOLLÁR**, Department of Structural Engineering, Budapest University of Technology and Economics, Műegyetem rkp. 3. K.II.42., 1521 BUDAPEST, Hungary, lkollar@eik.bme.hu

József **KÖVECSES**, Mechanical Engineering Department 817 Sherbrooke Street West, MD163 MONTREAL, Quebec H3A 2K6 jozsef.kovecses@mcgill.ca

Márta **KURUTZ**, Department of Structural Mechanics, Budapest University of Technology and Economics, Műegyetem rkp. 3, 1111 BUDAPEST, Hungary, kurutzm@eik.bme.hu

Lin **LU**, Center for Deepwater Engineering, Dalian University of Technology, Dalian, China lulin@dlut.edu.cn

Herbert **MANG**, Institute for Strength of Materials, University of Technology, Karlsplatz 13, 1040 VIENNA, Austria, Herbert.Mang@tuwien.ac.at

Sanjay **MITTAL**, Department of Aerospace Engineering, Indian Institute of Technology, KANPUR, UP 208 016, India, smittal@iitk.ac.in

Zenon **MRÓZ**, Polish Academy of Sciences, Institute of Fundamental Technological Research, Swietokrzyska 21, WARSAW, Poland zmroz@ippt.gov.pl

Gyula **PATKÓ**, Institute of Machine Tools and Mechatronics, University of Miskolc, H-3515 MISKOLC, Hungary, patko@uni-miskolc.hu

Jan **SLADEK**, Ústav stavbeníctva a architektúry, Slovenskej akadémie vied, Dubróvska cesta 9, 842 20 BRATISLAVA, Slovakia, usarslad@savba.sk

Gábor **STÉPÁN**, Department of Applied Mechanics, Budapest University of Technology and Economics, Műegyetem rkp. 3, 1111 BUDAPEST, Hungary, stepan@mm.bme.hu

Barna **SZABÓ**, Department of Mechanical Engineering and Materials Science, Washington University, Campus Box 1185, ST. LOUIS, MO 63130, USA, szabo@wustl.edu

Balázs **TÓTH**, Institute of Applied Mechanics, University of Miskolc, 3515 MISKOLC, Hungary, balazs.toth@uni-miskolc.hu

HONORARY EDITORIAL BOARD MEMBERS

Tibor **CZIBERE**, Department of Fluid and Heat Engineering, University of Miskolc, H-3515 Miskolc-Egyetemváros, Hungary

R. Ivan **LEWIS**, Room 2-16 Bruce Building, Newcastle University, NEWCASTLE UPON TYNE, NE1 7RU, UK

Gábor **HALÁSZ**, Department of Hydraulic Machines, Budapest University of Technology and Economics, Műegyetem rkp. 3, 1111 BUDAPEST, Hungary,

PREFACE

1. IN REMEMBRANCE OF PROFESSOR JÓZSEF FARKAS – A PROFESSIONAL LIFE DEDICATED TO STRUCTURAL OPTIMIZATION (15 DECEMBER 1927 – 15 SEPTEMBER 2016)

Professor Farkas graduated as a civil engineer from the Technical University of Budapest in 1950 and began teaching at the University of Miskolc. Between 1950-59 he taught at the Department of Mechanics and from 1959 at the Department of Materials Handling, now Department of Materials Handling and Logistics. In the past more than six decades, he developed courses on Metal Structures, Welded Structures and achieved an international reputation. The international novelty of these courses is that they are devoted to the design of structural components of machines and load-carrying structures. They consider dynamic effects, stiffness and vibration damping. These features made them suitable for the modular academic system of the Faculty of Mechanical Engineering and Informatics. The most important features of these courses consist in the application of mathematics, mechanics, optimization methods and applicability in the engineering practice. Optimum design provides a wide horizon, which is necessary for engineers. Based on Professor Farkas's work, the students of the faculty can obtain a comprehensive overview of the design of metal and welded structures.



Professor Farkas was one of the first who realized the importance of the application of computers in structural optimization. It must be pointed out that economic aspects are also considered in optimization by means of self-developed cost functions.

The theoretical calculations are complemented in most cases by experimental measurements carried out in laboratories, or in the field.

His complex approach resulting from the structural synthesis has had a great effect not only on his students, but also on his colleagues at the university and the engineers practicing in the industry.

In 1996 he retired and since 1998 he has been working as Professor emeritus, continuing his previous work unrelentingly. He gave lectures week by week, offered the students advice on their design assignments and guidance on writing theses. Related

to his tutorial activity he published a university textbook entitled *Metal Structures* in 1974. The second and revised edition came out in 1983. In 2016 a new textbook was published with Károly Jármai, entitled *Innovative Design of Metal Structures*.

About his teaching activity he was involved in the programs of welding engineers as well as in those offered to foreign students in English since beginnings. He joined the PhD training at the beginning and was the scientific advisor of several PhD students.

His scientific activity was continuous and undiminished for decades. He obtained his Ph.D. degree in 1966. His thesis was devoted to the design of stiffened plates. He obtained the title doctor of the Hungarian Academy of Sciences, i.e., the DSc degree, which is equivalent to the German habilitation, for a thesis on the optimum design of metal structures in 1978. After being revised and supplemented, his DSc thesis was published under the title *Optimum Design of Metal Structures* by Ellis Horwood, Chichester, UK and the Hungarian Publishing House Akadémiai Kiadó, Budapest in 1984. The book won a Hungarian Academy award.

His other books *Analysis and Optimum Design of Metal Structures*, and *Economic Design of Metal Structures*, were published by Balkema, and Millpress Science Publishers in Rotterdam, in 1997 and 2003, respectively. Later, two other books have been published: *Design and Optimization of Metal Structures*, by Horwood Publishers in 2008 and *Optimum Design of Steel Structures*, by Springer Verlag in 2013. His coauthor was one of his former students, Károly Jármai. Beside the books he has published about 250 papers and studies. Half of them were written in a foreign language, mainly in English. He read articles in five languages: English, German, Russian, Slovak, Polish. He held lectures also in English, German and Slovak languages.

His expertise was utilized by the industry as well. His main research areas are as follows: optimum design of metal structures, residual welding distortions and stresses, tubular structures, stiffened plates, sandwich structures, vibration damping and stability problems of steel structures.

His nearly seven-decade-long activity in the field of structural optimization should be especially highlighted. His optimum design methods can be used in other disciplines as well. He covered the application of design methods for various materials handling machines and equipment: cranes, crane runways, silos, bunkers, conveyor galleries, frames, cellular plates, tubular structures. In the field of machine tools, he also worked out a course for welded structures, mainly press frames.

His main external activities were in the Welding Division of the Scientific Society of Mechanical Engineers (GTE), the International Institute of Welding (IIW) and the International Society for Structural and Multidisciplinary Optimization (ISSMO). The Scientific Society of Mechanical Engineers awarded him the Pattantyús Medal. He was also awarded the Apáczai Csere János Award and the Memorial Medal of the 45-year-old Technical University of Kosice. He became Dr. Honoris Causa of the University of Miskolc in 2002.

He attended the Annual Assemblies of IIW and the symposia on Tubular Structures, organized by the Subcommission IIW XV-E for several years.

His international co-operation ranged from Japan to Canada. He established connections with professors from all over the world, as illustrated by the list of participants of the international conferences we have organized in the last 20 years.

His role in the Department of Materials Handling and Logistics was crucial. He was the head of the Division of Metal Structures. He was the scientific supervisor of several specialists in engineering optimization: Dr. habil. Imre Tímár, Prof. Károly Jármái, Ferenc Orbán, Sándor Rácz, László Szabó, Ferenc Szabó, György Kovács. He gave the first initiative for the research work of some professors, including the member of the Hungarian Academy of Sciences István Páczelt, Dr. habil. Mátyás Matolcsy and József Cselényi.

He was an excellent lecturer. He had the gift to present highly complicated ideas, relationships, lines of thoughts in an elegant and simple manner and to make his audience understand what at first seems to be difficult.

His personal hobby was listening to and playing classical music. He played baroque and classical music on the electronic organ. He published three books about baroque music and composers. He made four music CD-s, playing himself on a synthesizer.

All his former colleagues, students and co-workers remember Professor Farkas and keep him in their minds.

Miskolc, August 24, 2017

Károly Jármái

2. IN REMEMBRANCE OF PROFESSOR IMRE KOZÁK – A PROFESSIONAL LIFE
DEDICATED TO MECHANICS OF SOLID BODIES
(21 AUGUST 1930 - 17 NOVEMBER 2016)

Professor Kozák graduated from the University of Miskolc in 1954, was working for the university since then till his death. He chaired the Department of Mechanics from 1971 till 1993 and had a very significant influence on the scientific activity of the department in various ways: as a scientific leader of promising young PhD students and by starting a separate track in applied mechanics. He was a founder of JCAM and supported the journal in every possible way, which included reviewing a number of papers devoted to various problems in mechanics of solid bodies and he also did his best to find financial support so that we could come out as an open access journal. Volume 10, Number 2 in 2015 is dedicated to two excellent scientists: one of them is Professor Imre Kozák, who was 85 years old in that year. The Preface to that issue is a summary of his scientific carrier – we kindly refer our readers to that issue in which a detailed scientific biography can be found:

(<http://www.mech.uni-miskolc.hu/jcam/>).

Miskolc, September 21, 2017

György Szeidl

ASPECTS ON MODELING THE MECHANICAL BEHAVIOR OF ALUMINUM ALLOYS WITH DIFFERENT HEAT TREATMENTS

CAMELIA CERBU AND HORATIO TEODORESCU-DRAGHICESCU
Faculty of Mechanical Engineering, Transilvania University of Braşov
B-dul Eroilor 29, RO-500036, Braşov, ROMANIA
cerbu@unitbv.ro, draghicescu.teodorescu@unitbv.ro

[Received: April 25, 2017; Accepted: September 14, 2017]

Abstract. Mechanical characteristics of two kinds of the EN AW–6060 aluminum alloys were measured in tensile and three-point bending tests. Although there is a standard [20] that indicates the mechanical properties of the aluminum alloys used to manufacture different kinds of profiles, the main purpose of this paper is to compare the accuracy of the mechanical properties of the commercial aluminum alloy EN AW–6060 used to manufacture box profiles in T4 or T6 heat treatment conditions. It is shown that the maximum values σ_{\max} of the tensile and flexural stresses – these are denoted by σ_{\max} – are 41.55% and 75.12% greater for the EN AW–6060–T6 aluminum alloy than those for the EN AW–6060–T4 aluminum alloy. There are small differences concerning the modulus of elasticity E recorded: 7.52% for the case of Young’s modulus E in the tensile test; 5.34% for the modulus of elasticity in the three-point bending test. Both kinds of aluminum alloys have elastic-plastic behavior in tensile test. Theoretical concepts regarding the modeling of the nonlinear behavior of the elastic-plastic materials in the plastic range of the material are considered in order to simulate the behavior of the aluminum alloys in the tensile tests by using finite element analysis (FEA). Finally, we should remark that the $(\sigma - \varepsilon)$ stress-strain curves obtained in the numerical modeling match with those experimentally obtained for each aluminum alloy we have analyzed. Thus the input parameters for FEA (Young’s modulus E , the true stresses and strains belonging to the plastic range) for each type of aluminum alloy tested may be used in the case of any structural element made of such alloys.

Keywords: aluminum alloy, tensile test, bending test, heat treatment

1. NOMENCLATURE

Latin symbols

A_o	initial area of the cross-section of the tensile specimen,
A	instantaneous area of the cross-section of the tensile specimen at a certain time of loading in the plastic range
b, h	cross-sectional dimensions of the tensile and flexural specimens,
b, t	these subscripts indicate that the quantity considered was measured in the bending or tensile tests,

CV	coefficient of variation (or relative standard deviation) which is a standardized measure of dispersion; it is the ratio between Stdev and the average value of a set of values, expressed in percentage,
l_0, l	initial active length of the tensile specimen and the length of the specimen corresponding to the tensile force F ,
E	modulus of elasticity (Young's modulus),
F	tensile force in the tensile test / external force in the bending test,
p	intensity of the distributed forces acting on the free end of the tensile specimen in FEA,
Stdev	standard deviation of a data set,
$T4, T6$	heat treatment conditions of the aluminum alloy
V_0, V	volume of the specimen at the beginning of the tensile test and at time t ,
W	work done until maximum load is reached.

Greek symbols

Δl_{\max}	elongation of the tensile specimen at maximum load,
$\varepsilon, \varepsilon_{\log}$	engineering and logarithmic strains,
ε_{\max}	maximum strain,
ε_x	strain on the longitudinal axis Ox of the tensile specimen,
σ_{\max}	maximum stress,
σ_r	true tensile stress,
σ_x	normal stress on the longitudinal axis Ox of the tensile specimen,
$(\sigma_r - \varepsilon_r)$	true stress strain curve in tensile loading.

2. INTRODUCTION

The effects of the microstructure as well as the effects of heat and ageing treatments on the mechanical properties of aluminum alloys are presented in references [1–7]. New aluminum alloys have been developed for automotive applications in the last years. Aluminum alloys exhibit an excellent combination of strength and ductility [8]. Different homogenizing, annealing and aging processes of various aluminum alloys have been also investigated [9–11]. Hardness, yield strength and ultimate tensile strength of the AA6063 aluminum alloy after two-stage solution treatment were significantly increased, while elongation to failure remained unchanged [12]. Porosity evaluation on the fracture surfaces of AlSi10MnMg(Fe) secondary alloys was investigated showing an increasing of the porosity at these surfaces [13]. Fatigue and mechanical behaviors at high temperatures during welding of different kinds of aluminum alloys are presented in [14–16]. The influence of the composition of the aluminum alloy and the heat treatment on their mechanical properties resulted in, for instance, a high rate change in hardness during quick cooling [17, 18]. The effects of the different treatments on the mechanical properties and the microstructure of Al-Zn-Mg(-Cu) based aluminum alloys are also discussed in [19].

The main purpose of the present paper is to show the effects of thermal treatment on the mechanical properties of the EN AW-6060 AlMgSi aluminum alloy using tensile specimens cut from extruded box profiles. The alloy EN AW-6060 AlMgSi is a widely used extrusion alloy. It is recommended for applications such as the following: frame

profiles for windows, doors, curtain walls, fences, railings, stairs, frame systems for interior accessories, pneumatic equipment, irrigation pipes and pipes for cooling.

Another goal is to define the input parameters for the finite element analysis (FEA) by using the experimental results in order to model the nonlinear behavior of the aluminum alloy for any structure and/or any structural element made of such an alloy. For this purpose we compare the stresses and strains in the tensile specimens determined by the finite element method with the values experimentally obtained in the tensile tests. The input material parameters for FEA are: Young's modulus experimentally obtained from the tensile tests in order to model the behavior of the aluminum in the elastic range and the true stress σ_r and true strain ε_r value pairs computed using experimental results in order to properly model the material behavior of the aluminum in the plastic range. A British standard gives the mechanical properties for the extruded rod/bar, tube and profiles made of aluminum alloys [20].

In order to show the effects of the thermal treatment on the EN AW-6060 AlMgSi aluminum alloy, two kinds of this alloy were tested: the EN AW-6060-T4-aluminum alloy in T4 heat treatment condition and the EN AW-6060-T6-aluminum alloy in T6 heat treatment condition. The T4 heat treatment condition corresponds to naturally aged to a stable condition while T6 heat treatment condition corresponds to solution heat treated, quenched and artificially aged [21].

3. THEORETICAL ISSUES

It is known that aluminum has elastic-plastic behavior under mechanical load. It should, therefore, be taken into account that a decreasing of the cross-section A takes place in the plastic range of loading as the tensile force F increases. In the plastic range, it is customary to define a logarithmic strain ε_{\log} by the following relationship [22]:

$$\varepsilon_{\log} = \int_{l_0}^l \frac{dl}{l} \tag{1}$$

where l_0 is the initial active length of the tensile specimen and is the length of the specimen corresponding to the tensile force. The logarithmic strain (1) is a nonlinear function of the length l . The following relation follows from (1) between the logarithmic strain ε_{\log} and the engineering strain ε [22]:

$$\varepsilon_{\log} = \ln \frac{l}{l_0} = \ln \frac{l_0 + \Delta l}{l_0} = \ln (1 + \varepsilon). \tag{2}$$

The stress that corresponds to the logarithmic strain ε_{\log} is the true tensile stress:

$$\sigma_r = F/A \tag{3}$$

where A is the instantaneous area of the cross-section in the tensile specimen.

In the case of nonlinear material behavior we shall assume that the volume of the tensile specimen remains unchanged:

$$V = V_0, \quad \Rightarrow \quad Al = A_0l_0. \tag{4}$$

Hence

$$A = \frac{A_0 \cdot l_0}{l} = \frac{A_0}{\frac{l}{l_0}} = \frac{A_0}{1 + \varepsilon}. \quad (5)$$

Substituting (5) into (3), we obtain the following relation between the true stress σ_r and the engineering stress σ [22]:

$$\sigma_r = \frac{F}{A} = \frac{F(1 + \varepsilon)}{A_0} \Rightarrow \sigma_r = \sigma(1 + \varepsilon). \quad (6)$$

The true stress-strain curve $\sigma_r - \varepsilon_r$ can be drawn by using the true values of the stresses σ_r and logarithmic strains ε_{\log} computed on the basis of relations (2) and (6).

4. MATERIALS AND WORK METHOD

4.1. Materials. In accordance with European Standard SR-EN 573 – 3 / 2010 [24], EN AW–6060 aluminum alloy belongs to the series 6000 of the aluminum alloys AlMgSi (aluminum–magnesium–silicon). Chemical composition of the aluminum alloy EN AW 6060 is: 0.3-0.6% Si; 0.1-0.3% Fe; 0.10% Cu; 0.35-0.60 % Mg; 0.05 % Cr; 0.15% Zn; 0.10 % Ti; 0.05 % other metallic components so as not to exceed 0.15%; the difference is covered by the aluminum [24]. According to [25] the EN AW–6060 aluminum alloy in T4 or T6 heat treatment condition are encoded as: EN AW–6060-T4 or EN AW–6060-T6, respectively.

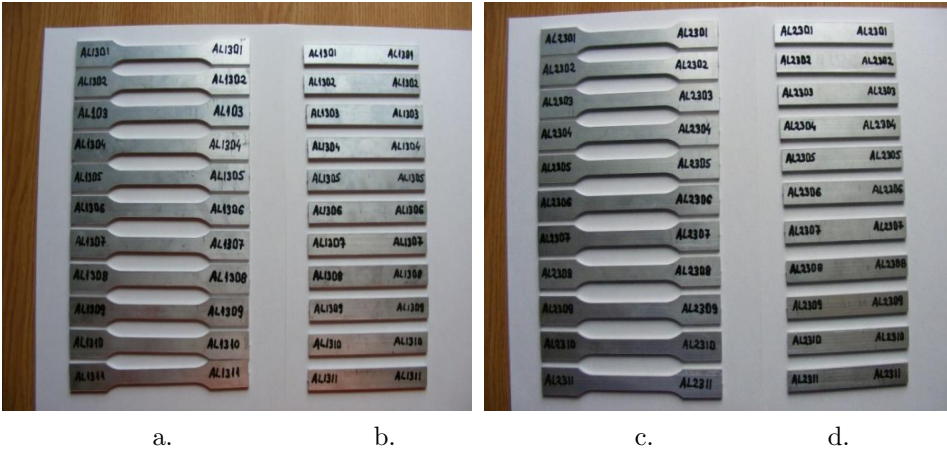


Figure 1. Specimens for testing: a, b - Tensile/flexural specimens made of aluminum alloy EN AW–6060–T4; c, d - Tensile/flexural specimens made of aluminum alloy EN AW–6060–T6

The tensile specimens shown in Figure 1a and c are manufactured according to European Standard EN ISO 6892-1: 2002 [26]. Some dimensions of the tensile specimen are: total length – 150 mm, active length $l_0 = 60$ mm, the width of the active length is $b = 10$ mm, the width of end part that is clamped in the tensile machine is $B = 20$ mm.

The flexural specimens shown in Figure 1b and d have 120 mm in length and the width of the rectangular cross-section is 15 mm. The thickness is 3 mm for both kinds of specimens.

The tensile and flexural specimens are cut from commercial profiles having a box cross-section and made of EN AW-6060 aluminum alloy which was subjected to two different heat treatment conditions (T4 and T6).

4.2. Work method.

4.2.1. *Experimental methods.* For the tensile tests we used a tensile machine manufactured by LLOYD Instruments (West Sussex, United Kingdom). Its maximum load capacity is ± 50 kN. The speed of loading was 3 mm/min in accordance with the European Standard EN ISO 6892-1: 2002 [26]. An extensometer was used in order to record the elongation of the specimen. The initial span between the marks of the tensile specimen that is the initial active length was equal to 50 mm [26].

A LR5K Plus machine manufactured by LLOYD Instruments (West Sussex, United Kingdom) was used for the three-point bending test. Its maximum load capacity is ± 15 kN. The flexural specimen was simply supported at its ends during testing and the span between the supports was equal to 80 mm. The crosshead speed was 15 mm/min.

4.2.2. *Theoretical investigations.* Finite element analysis (FEA) was used to simulate the mechanical behavior of the aluminum tensile specimen in the tensile test. The main objective of FEA was to compare the stress-strain curve obtained for the element located at the middle of the specimen with the experimentally obtained stress-strain curve. Consequently, the graph of the true stress-strain curve ($\sigma_r - \varepsilon_r$) will be the output result presented in Subsection 5.3 Theoretical versus experimental results. If the theoretical curve matches with the experimental one, the input parameters of the material used in FEA can also be used for any structure made of such kinds of aluminum. Another goal of FEA is to compare the maximum theoretical value of the tensile stress σ_{\max} obtained from the finite element model (FEM) with the value recorded in the tensile test.

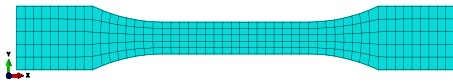


Figure 2. Finite element model (FEM)



Figure 3. Boundary conditions and load applied

The geometrical model for the finite element analysis of the tensile specimen was designed in accordance with the dimensions specified in [26] and also used to manufacture the tensile specimens. The finite element model (FEM) is shown in Figure 2. Four-node plane stress finite elements were applied to numerically model the stress and strain states in the tensile specimen. Figure 3 shows the boundary conditions applied (one end of the specimen is fixed) and the distributed force p exerted on the other end of the tensile specimen.

Two different cases were considered in the finite element analysis concerning the properties of the material assigned to the models of the tensile specimens: 1) properties of the EN AW-6060-T4 aluminum alloy; 2) properties of the EN AW-6060-T6 aluminum alloy.

The material input parameters used in FEA are based both on the experimental results obtained in tensile tests and on the quantities computed by using relations (2) and (6) in order to model the elastic-plastic behavior of the aluminum alloy in each case. Therefore, Young's modulus E experimentally obtained in tensile test was an input data for the finite element analysis to model the material behavior of the aluminum in the elastic range of the stress-strain curve ($\sigma - \varepsilon$). To model the mechanical behavior in the plastic range of the stress-strain curve ($\sigma - \varepsilon$), we used the true stress σ_r and true strain ε_r value pairs computed by utilizing relations (2) and (6), respectively. The average stress-strain curves ($\sigma - \varepsilon$) calculated from the experimentally recorded stress strain curves (see Figure 4) were also considered as input data for each aluminum alloy in order to describe their mechanical behavior in the plastic range.

The value of the Poisson coefficient ν was set at $\nu = 0.33$ for the EN AW-6060 aluminum alloy according to [27].

The dimensions for the geometrical models of the tensile specimens were the same as those of tensile specimens in the tensile tests.

In this way we can compare the stress and strain states obtained from the finite element computations or the experiments for each aluminum alloy.

Finally, the true stress-strain curve ($\sigma_r - \varepsilon_r$) obtained from finite element analysis FEA analysis, which is based on theoretical concepts presented in Section 2, is compared with the conventional stress-strain curves ($\sigma - \varepsilon$) recorded in the tensile tests of each aluminum alloy.

5. RESULTS

5.1. Experimental results. The stress-strain curves ($\sigma - \varepsilon$) recorded in tensile tests are shown in Figure 4. Note that after the yield point, the curves ($\sigma - \varepsilon$) corresponding

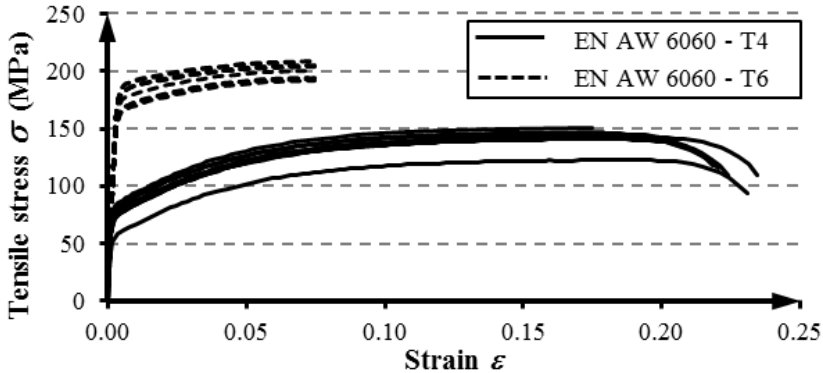


Figure 4. Stress strain curve ($\sigma - \varepsilon$) recorded in the tensile test

to the EN AW-6060-T4 aluminum alloy are located above the stress strain curves of the EN AW-6060-T6 aluminum alloy. This remark shows that the maximum value of the tensile stress σ_{\max} is greater for the EN AW-6060-T6 aluminum alloy than for the EN AW-6060-T4 aluminum alloy. But the maximum axial strain $\varepsilon_{t \max}$ recorded at the maximum force F_{\max} is less for the EN AW-6060-T6 aluminum alloy than for the EN AW-6060-T4 aluminum alloy.

Table 1. Mechanical properties for material EN AW-6060-T4 in tensile test

No. of the tensile specimen	Width b (mm)	Thickness h (mm)	Young's modulus E (MPa)	Maximum load (N)	Max. tensile stress $\sigma_{t \max}$ (MPa)	Elongation at max. load Δl_{\max} (mm)	Max. strain at max. load $\varepsilon_{t \max}$	Work to max. load W_t (Nmm)
1	10.03	3.00	64637	3689	123	9.307	0.186	30110
2	10.02	3.00	49239	4253	142	8.576	0.172	32164
3	10.04	2.98	60051	4364	146	7.961	0.159	30701
4	10.03	2.97	69708	4233	142	9.855	0.197	37372
5	10.03	2.97	68511	4196	141	9.321	0.186	34841
6	10.04	3.00	41589	4429	147	8.751	0.175	34608
7	10.02	2.98	69443	4277	143	9.874	0.197	37969
8	10.02	3.00	35984	4308	143	9.940	0.199	38553
9	10.02	2.96	66626	4480	151	8.561	0.171	34147
10	10.03	2.96	57231	4195	141	8.632	0.173	31924
Average value	10.03	2.98	58302	4242	142	9.078	0.182	34239
Stdev	0.008	0.017	12164	217	7.36	0.68	0.014	3020
CV	0.08%	0.57%	20.86%	5.12%	5.18%	7.49%	7.69%	8.82%

Table 2. Mechanical properties for material EN AW-6060-T6 in tensile test

No. of the tensile specimen	Width b (mm)	Thickness h (mm)	Young's modulus E (MPa)	Maximum load (N)	Max. tensile stress $\sigma_{t \max}$ (MPa)	Elongation at max. load Δl_{\max} (mm)	Max. strain at max. load $\varepsilon_{t \max}$	Work to max. load W_t (Nmm)
1	10.10	3.08	54394	6040	194	3.759	0.075	21198
2	10.12	3.10	50549	6420	205	4.396	0.088	26735
3	10.08	3.06	55699	6443	209	3.842	0.077	23379
4	10.08	3.09	55275	6489	208	4.126	0.083	25376
5	10.08	3.06	52199	6192	201	3.642	0.073	21064
6	10.07	3.07	55148	5988	194	4.650	0.093	26403
7	10.08	3.03	55699	6291	206	4.404	0.088	26244
8	10.04	3.07	58855	6330	205	4.359	0.087	26192
9	10.06	3.09	54329	6028	194	4.280	0.086	24257
10	10.10	3.08	47042	5960	192	4.078	0.083	24365
Average value	10.08	3.07	53919	6218	201	4.154	0.083	24365
Stdev	0.022	0.020	3267	203	6.65	0.32	0.006	2161
CV	0.22%	0.65%	6.06%	3.26%	3.31%	7.70%	7.23%	8.87%

The average values of the mechanical properties recorded in tensile test are shown in Tables 1 and 2 for both tested alloys. The average value of Young's modulus E , which is 58302 MPa for the aluminum alloy EN AW-6060-T4, is greater by 8.13% than that for the aluminum alloy EN AW-6060-T6, which is 5319 MPa. The maximum value of the tensile stress $\sigma_{t \max}$ is greater by 41.55% for the EN AW-6060-T6 alloy than for the EN AW-6060-T4 alloy – compare the values 201 MPa and 142 MPa. The maximum strain $\varepsilon_{\max} = 0.182$, which was recorded at the maximum force F_{\max} , is greater by 119.28% for EN AW-6060-T4 than for EN AW-6060-T6 since the latter is 0.083. This is the reason why the work done till we reach the maximum load is greater by 40.52% for the EN AW-6060-T4 aluminum alloy than the value recorded for the EN AW-6060-T6 alloy.

Analyzing the coefficients of variation CV corresponding to Young's modulus, we got $CV=20.86\%$ which shows more variability of the data set of the EN AW 6060 alloy in T4 heat treatment condition (Table 1). The reason for this is, in all probability, the slipping of some tensile specimens in the grip elements of the tensile machine. The coefficient $CV=6.06\%$ is, however, closer to 5% in the case of the EN AW-6060-T6 alloy (Table 2).

As regards the maximum tensile stress, the computed coefficients of variation CV are acceptable because these are equal to 5.18% and 3.31% for the cases of T4 and T6 heat treatment conditions, respectively. This shows less variability of the data set – see again Tables 1 and 2.

The stress-strain curves ($\sigma - \varepsilon$) recorded in the three-point bending test are shown in Figure 5. The curves are shown graphically for the points located at the bottom of the critical cross-section of the flexural specimen (cross-section located at midpoint of the span between supports). The values of the engineering stresses and strains are computed and recorded in a text file, in real-time, by the LR5K Plus machine used for the bending test. Engineering stresses σ and strains ε depend both on the initial dimensions b, h of the flexural specimen and the span between the supports (this is 80 mm) that were entered in the software of the machine before testing.

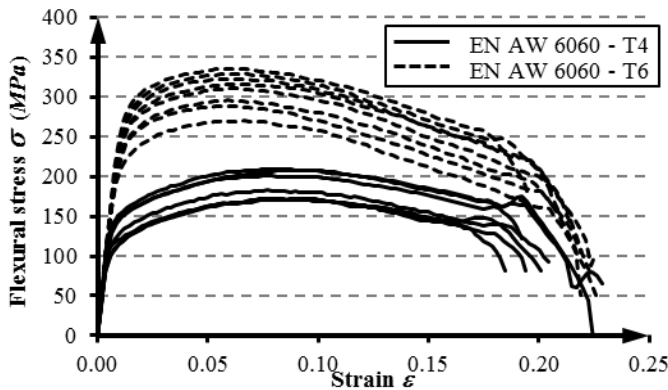


Figure 5. Stress strain curve ($\sigma - \varepsilon$) recorded in the three point bending test

We may observe in Figure 5 that the slopes of the elastic portions of the $(\sigma - \varepsilon)$ curves are greater in the case of the EN AW-6060-T6 aluminum alloy. The $(\sigma - \varepsilon)$ curves for the EN AW-6060-T6 alloy are located above the curves that belong to the other aluminum alloy which is in T4 heat treatment condition. Hence it follows that the modulus of elasticity E in the bending test and the maximum stress $\sigma_{b \max}$ – both in the case of EN AW-6060-T6 aluminum alloy – are greater than the same values recorded for the other material, i.e., for the EN AW-6060-T4 aluminum alloy (the cross section is the same as before).

Table 3. Mechanical properties for the material EN AW-6060-T4 in the three-point bending test

No. of the flexural specimen	Width b (mm)	Thick-ness h (mm)	Modulus of elasticity in bending test E (MPa)	Max. force F_{\max} (N)	Max. stress at max. load $\sigma_{b \max}$ (MPa)	Max. strain at max. load $\varepsilon_{b \max}$	Work to max. load W_b (Nmm)
1	14.99	3.03	24195	210	183	0.080	5072
2	14.97	3.01	25094	235	210	0.081	5832
3	14.98	2.98	28726	191	173	0.078	4535
4	14.96	3.02	26324	228	201	0.075	5228
5	14.97	3.03	24380	196	171	0.092	5431
6	14.97	3.00	24003	193	172	0.092	5431
7	15.03	3.01	23939	236	208	0.091	6581
Average value	14.98	3.01	25237	213	188	0.084	5449
Stdev	0.023	0.018	1751	20	17.55	0.007	640
CV	0.15%	0.60%	6.94%	9.39%	9.34%	8.33%	11.75%

Table 4. Mechanical properties for the material EN AW-6060-T6 in the three-point bending test

No. of the flexural specimen	Width b (mm)	Thick-ness h (mm)	Modulus of elasticity in bending test E (MPa)	Max. force F_{\max} (N)	Max. stress at max. load $\sigma_{b \max}$ (MPa)	Max. strain at max. load $\varepsilon_{b \max}$	Work to max. load W_b (Nmm)
1	14.98	3.11	26282	349	289	0.055	5531
2	15.01	3.12	26515	360	296	0.057	5916
3	15.00	3.11	26303	382	316	0.056	6164
4	15.00	3.11	26523	390	323	0.059	6770
5	15.02	3.11	27389	406	336	0.062	7460
6	14.98	3.11	26502	375	311	0.060	5715
7	15.01	3.11	27356	327	270	0.060	5715
8	14.97	3.11	25801	398	330	0.058	6681
Average value	15.00	3.11	26584	373	309	0.058	6345
Stdev	0.018	0.004	540	27	22.39	0.002	637
CV	0.12%	0.13%	2.03%	7.24%	7.25%	3.45%	10.04%

5.2. Theoretical results. In the present section it is our aim to determine the stress and strain states in the tensile specimens for those two cases when the material properties are different from each other, i.e., for the EN AW-6060-T4 and EN AW-6060-T6 aluminum alloys. The tensile stress σ_x and axial strain ε_x distributions for the EN AW-6060-T4 aluminum alloy are shown in Figure 6a and b as functions of the plane coordinates of x, y provided that the applied $F = 74196$ N axial force is the maximum value of the axial forces experimentally recorded in the case of those tensile specimens whose $(\sigma - \varepsilon)$ stress-strain curves were considered to determine the behavior of this kind of alloy in the plastic range. It is worth of mentioning that the maximum tensile stress $\sigma_{\max} = 140.1$ MPa (see Figure 6a) obtained from the finite element analysis is approximately equal to the average value 142 MPa obtained from the experiments (Table 1).

In the same manner, Figure 7 shows the distributions of the tensile stresses and strains regarding the case of the other material, i.e., for the EN AW-6060-T6 aluminum alloy. The maximum tensile stress (Figure 7a) obtained from the finite element analysis is again approximately equal to the average value of the experimental results (Table 2).

In Figures 6 and 7, the plots that depicts the un-deformed and deformed shapes of the tensile specimen are overlapped in order to highlight the elongation and the transversal contraction. It has to be noted that the deformation scale factor is equal to 5 in the case of the plots.

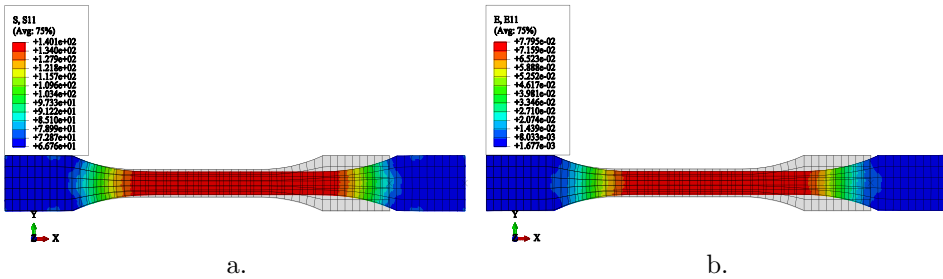


Figure 6. FEA results for material properties EN AW-6060-T4 aluminum alloy: a. Stress; b. Strain

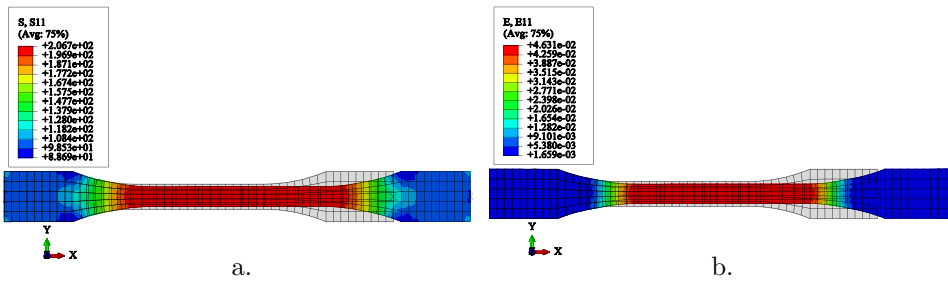


Figure 7. FEA results for material properties EN AW-6060-T6 aluminum alloy: a. Stress; b. Strain

It can be mentioned again that although the axial force F applied to the EN AW-6060-T6 aluminum specimen is greater by 47.57% than the axial force applied to EN AW-6060-T4 aluminum specimen, the maximum strain $\varepsilon_{x \max} = 4.631 \times 10^{-2}$ recorded for the EN AW-6060-T6 aluminum specimen is smaller by 40.59% than the same quantity for the other aluminum alloy.

5.3. Theoretical versus experimental results. In every case we analyzed, the true stress-strain curve ($\sigma_r - \varepsilon_r$) obtained from the finite element analysis was compared to the stress-strain curve ($\sigma - \varepsilon$) experimentally determined. The stress-strain curve ($\sigma - \varepsilon$) was also used to determine the material behavior in the plastic range.

Figure 8a shows comparisons between the stress-strain curve ($\sigma_r - \varepsilon_r$) of the finite element model and the experimentally recorded stress-strain curve valid for the EN AW-6060-T4 aluminum specimen. A similar comparison is made in Figure 8b for the EN AW-6060-T6 aluminum specimen.

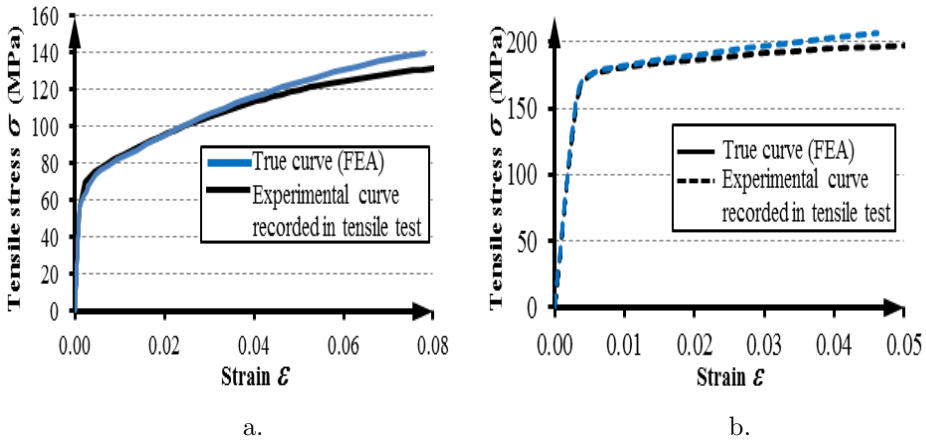


Figure 8. Comparison of the true and experimental stress-strain curves recorded in tensile tests for a. EN AW-6060-T4 aluminum alloy; b. EN AW-6060-T6 aluminum alloy

Figures 8a and 8b show a good fit between both kinds of stress-strain curves. We may therefore come to the conclusion that the material properties of the two aluminum alloys are well-determined for the numerical models of the tensile specimens from the elastic and the plastic point of views as well.

6. CONCLUSION

We remark that the mechanical properties recorded for the EN AW-6060-T6 aluminum alloy are generally greater than the values recorded for the EN AW-6060-T4 aluminum alloy.

The maximum values of the tensile and flexural stresses (σ_{\max}) are 41.55% and 75.12% greater in the case of the EN AW-6060-T6 aluminum alloy than in the case of the EN AW-6060-T4 aluminum alloy. With regard to these strength properties, the

aluminum EN AW-6060 box profiles in T6 heat treatment condition are recommended instead of the aluminum EN AW-6060 box profiles that are in T4 heat treatment condition in order to manufacture structures and/or structural elements for which high strength is a fundamental requirement.

It is worth of mentioning that the EN AW-6060 aluminum alloy has large plastic deformations in the three-point bending test independently of the heat treatment it was subjected to (Figure 5).

A similar remark can be may made for the EN AW-6060-T4 alloy in the case of the tensile test. The maximum strain ε_{\max} recorded at the maximum force F_{\max} is more than twice as high (by 119.28%) for the EN AW-6060-T4 alloy ($\varepsilon_{\max} = 0.182$) than for the EN AW-6060-T6 alloy ($\varepsilon_{\max} = 0.083$). These remarks lead to the conclusion that the EN AW-6060-T4 aluminum alloy in T4 heat treatment condition is a ductile material.

The good fit between the $\sigma_r - \varepsilon_r$ stress-strain curve computed using the critical finite element of the finite element model and the $\sigma_r - \varepsilon_r$ stress-strain curve obtained experimentally let us conclude that the way we used for determining the material properties is validated for both kinds of aluminum alloys involved in this research.

Moreover, in future research the input parameters determined for FEA (Young's modulus E , the true stress σ_r and true strain ε_r value pairs to determine the material behavior in the plastic range) in the case of the EN AW-6060 aluminum alloy in T4 or T6 heat treatment condition can also be used to determine the material properties for a FEA concerning any mechanical structure and/or structural element made of such aluminum alloy.

Acknowledgement. The authors hereby acknowledge the structural fund project PRO-DD (POS-CCE, O.2.2.1., ID 123, SMIS 2637, ctr. No 11/2009) and the Transylvania University of Braşov for providing the infrastructure used in this work.

REFERENCES

1. CHEN, R., XU, Q., GUO, H., XIA, Z., WU, Q. and LIU, B.: Correlation of solidification microstructure refining scale, Mg composition and heat treatment conditions with mechanical properties in Al-7Si-Mg cast aluminum alloys. *Materials Science and Engineering A*, **685**, (2017), 391-402.
2. JUNG, J. G., LEE, J. M., CHO, Y. H. and YOON, W. H.: Combined effects of ultrasonic melt treatment, Si addition and solution treatment on the microstructure and tensile properties of multicomponent AlSi alloys. *Journal of Alloys and Compounds*, **693**, (2017), 201-210.
3. PENG, Y., LI, S., DENG, Y., ZHOU, H., XU, G. and YIN, Z.: Synergetic effects of Sc and Zr microalloying and heat treatment on mechanical properties and exfoliation corrosion behavior of Al-Mg-Mn alloys. *Materials Science and Engineering: A*, **666**, (2016), 61-71.
4. LEE, Y. S., CHA, J. H., KIM, S. H., LIM, C. Y. and KIM, H.W.: Effect of pre-homogenization deformation treatment on the workability and mechanical properties of AlMg5Si2Mn alloy. *Materials Science and Engineering: A*, **685**, (2017), 244-252.

5. ABOULKHAIR, N. T., MASKERY, I., TUCK, C., ASHCROFT, I. and EVERITT, N. M.: Improving the fatigue behaviour of a selectively laser melted aluminum alloy: Influence of heat treatment and surface quality. *Materials & Design*, **104**, (2016), 174-182.
6. DING, J. K., WANG, D. P., WANG, Y. and DU, H.: Effect of post weld heat treatment on properties of variable polarity TIG welded AA2219 aluminum alloy joints. *Transactions of Nonferrous Metals Society of China*, **24**(5), (2014), 1307-1316.
7. ZHONG, H., ROMETSCH, P. and ESTRIN, Y.: Effect of alloy composition and heat treatment on mechanical performance of 6xxx aluminum alloys. *Transactions of Nonferrous Metals Society of China*, **24**(7), (2014), 2174-2178.
8. LI, Q., LI, F., XIA, T., LAN, Y., JIAN, Y. and TAO, F.: Effects of in-situ γ -Al₂O₃ particles and heat treatment on the microstructure and mechanical properties of A356 aluminum alloy. *Journal of Alloys and Compounds*, **627**, (2015), 352-358.
9. LU, Y., WANG, J., LI, X., CHEN, Y., ZHOU, D., ZHOU, G. and XU, W.: Effect of pre-deformation on the microstructures and properties of 2219 aluminum alloy during aging treatment. *Journal of Alloys and Compounds*, **699**, (2017), 1140-1145.
10. ASHRAFIZADEH, S. M., EIVANI, A. R., JAFARIAN, H. R. and ZHOU, J.: Improvement of mechanical properties of AA6063 aluminum alloy after equal channel angular pressing by applying a two-stage solution treatment. *Materials Science and Engineering: A*, **687**, (2017), 54-62.
11. NIKLAS, A., ORDEN, S., BAKEDANO, A., DA SILVA, M., NOGUÉS, E. and FERNÁNDEZ-CALVO, A. I.: Effect of solution heat treatment on gas porosity and mechanical properties in a die cast step test part manufactured with a new AlSi10MnMg(Fe) secondary alloy. *Materials Science and Engineering: A*, **667**, (2016), 376-382.
12. AKHIL, K.T., ARUL, S. and SELLAMUTHU, R.: The effect of heat treatment and aging process on microstructure and mechanical properties of A356 aluminum alloy sections in casting. *Procedia Engineering*, **97**, (2014), 1676-1682.
13. YANG, H., JI, S. and FAN, Z.: Effect of heat treatment and Fe content on the microstructure and mechanical properties of die-cast Al-Si-Cu alloys. *Materials & Design*, **85**, (2015), 823-832.
14. MAISONNETTE, D., SUERY, M., NELIAS, D., CHAUDET, P. and EPICIER T.: Effects of heat treatments on the microstructure and mechanical properties of a 6061 aluminum alloy. *Materials Science and Engineering: A*, **528**(6), (2011), 2718-2724.
15. SHIN, J., KIM, T., KIM D. E., KIM, D. and KIM, K.: Castability and mechanical properties of new 7xxx aluminum alloys for automotive chassis/body applications. *Journal of Alloys and Compounds*, **698**, (2017), 577-590.
16. GEETHA, B. and GANESAN, K.: The effects of aging temperature and time on mechanical properties of A356 aluminum cast alloy with red mud addition and treated by T6 heat treatment. *Materials Today: Proceedings*, **2**(4-5), (2015), 1200-1209.
17. MAISONNETTE, D., BARDEL, D., ROBIN, V., NELIAS, D. and SUERY, M.: Mechanical behavior at high temperature as induced during welding of a 6xxx series aluminum alloy. *International Journal of Pressure Vessels and Piping*, **149**, (2017), 55-65.
18. ROMETSCH, P. A., ZHANG, Y. and KNIGHT, S.: Heat treatment of 7xxx series aluminum alloys—Some recent developments. *Transactions of Nonferrous Metals Society of China*, **24**(7), (2014), 2003-2017.

19. ROBINSON, J. S. and REDINGTON, W.: The influence of alloy composition on residual stresses in heat treated aluminum alloys. *Materials Characterization*, **105**, (2015), 47-55.
20. BS EN 755-2: 1997. Aluminium and aluminum alloys – Extruded rod/bar, tube and profiles. Part 2: Mechanical properties. 1997.
21. BS EN 515:1993. Aluminium and aluminum alloys. Wrought products. Temper designations. Standard by British-Adopted European Standard, 10/15/1993.
22. SANTAJOJA, K.: Viscous and elastic-plastic material model in the ABAQUS. *Metal laboratory. VTT Publications 144, Technical Research Centre of Finland Espoo*, 1993, pp. 3-54. ISBN 951-38-4382-3, ISSN 1235-0621.
23. WANG, B., CHEN, X. H, PAN, F. S., MAO J. J. and FANG, Y.: Effects of cold rolling and heat treatment on microstructure and mechanical properties of AA 5052 aluminum alloy. *Transactions of Nonferrous Metals Society of China*, **25**(8), (2015), 2481-2489.
24. SR EN 573-3: 2010. Aluminium and aluminum alloys. Chemical composition and form of wrought products. Part 3: Chemical composition and form of products. Romanian Standard version, ASRO, 2010.
25. SR EN 573-5: 2008. Aluminium and aluminum alloys. Chemical composition and form of wrought products. Part 5: Codification of standardized wrought products. Romanian Standard version, ASRO, 2008.
26. SR EN ISO 6892-1: 2010 (or EN ISO 6892-1: 2002). Metallic materials. Tensile testing. Part 1: Method of test at room temperature.
27. <http://www.euralliage.com/6060.htm>

UNSTEADY MHD FREE CONVECTIVE HEAT AND MASS TRANSFER FLOW WITH VARIABLE HEAT AND MASS FLUXES

CHAVI MAHESHWARI, GOVIND PATHAK
Department of Mathematics, Radha Govind Engineering College
Garh Road, Meerut (U.P), 250004, India
chhavi.rathi@gmail.com, pathakgovind@Rediffmail.com

S. P. GUPTA
B.S.A. College, Mathura (U.P), India

[Received: March 15, 2017; Accepted: July 12, 2017]

Abstract. The mass, momentum and heat transfer in unsteady free convection flow along an infinite porous vertical plate, suddenly set in uniform motion with variable heat and mass fluxes at the plate, in the presence of uniform transverse magnetic field fixed to the plate, has been investigated. Similar solutions of energy and concentration boundary layer equations, for a particular form of suction/injection velocity $v_w(t)$, is obtained. For solution of the momentum boundary layer equation, a series expansion of velocity function in powers of product of magnetic field parameter and time is assumed. The analytical solutions of resulting ordinary differential equations have been obtained in terms of repeated integrals of complementary error functions. Also, the velocity, temperature and concentration profiles have been drawn and discussed.

Keywords: boundary layer flow, free convection, heat and mass flux, mass transfer, skin friction coefficient

1. INTRODUCTION

Elbashbeshy [1] and Pohlhausen [2] have free convection flow of fluids past a semi-infinite isothermal vertical plate in presence of magnetic field. Mohsin and Mandal [3], Dave et al. [4] and Pathak and Tak [5] have studied the unsteady free convection flow along an accelerated infinite porous plate, in presence of a transverse magnetic field, fixed relative to fluid. Soundalgekar [6], Tak and Pathak [7] and Tak and Sisodia [8] studied the same problem for the magnetic field fixed relative to the plate. In the present problem unsteady mass, momentum and heat transfer are investigated in free convection flow of binary fluids along a vertical porous plate suddenly set in uniform motion in its own plane, with variable heat and mass fluxes in presence of transverse magnetic field fixed to the plate.

2. MATHEMATICAL FORMULATION AND ANALYSIS

Consider an unsteady flow of an incompressible electrically conducting fluid in the presence of foreign species along an infinite vertical porous non-conducting plate in presence of uniform transverse magnetic field. At time $t' \leq 0$ the temperature and foreign species concentration at the plate and the fluid are assumed to be T'_∞ and c'_∞ , respectively. For $t' > 0$, the plate temperature and species concentration at the plate are instantaneously raised such that there is a variable heat flux q'_∞ per unit area and variable mass flux m_w per unit area from the plate moves upwards in its own plane and is maintained at uniform velocity u'_0 . The transverse magnetic field is assumed to be fixed relative to the plate. The axis x' is taken along the plate in upward direction and the axis y' is normal to it. For a small concentration level, the Soret-Dufour effects can be neglected in the energy equation. The electrical conductivity of the fluid is assumed to be small so that the induced magnetic field can be neglected in comparison of applied magnetic field. Then, under the usual Boussinesq's approximations, equations governing the flow in absence of frictional heating are (Gebhart [9]):

$$\frac{\partial v'}{\partial y'} = 0 \Rightarrow v' = v'_\omega(t'), \quad (1)$$

$$\frac{\partial u'}{\partial t'} + v' \frac{\partial u'}{\partial y'} = \nu \frac{\partial^2 u'}{\partial y'^2} + g\beta(T' - T'_\infty) + g\beta^*(c' - c'_\infty) - \frac{\sigma B_0^2(u' - u'_0)}{\rho}, \quad (2)$$

$$\frac{\partial T'}{\partial t'} + v' \frac{\partial T'}{\partial y'} = \frac{k}{\rho c_p} \frac{\partial^2 T'}{\partial y'^2}, \quad (3)$$

$$\frac{\partial c'}{\partial t'} + v' \frac{\partial c'}{\partial y'} = D \frac{\partial^2 c'}{\partial y'^2}, \quad (4)$$

where u' and v' are longitudinal and normal components of velocity respectively, ν is the kinematic viscosity, T' is the temperature, c' is the concentration, D is the coefficient of mass diffusion, g is the gravitational acceleration, β is the coefficient of thermal expansion, β^* is the coefficient of species concentration expansion, k the thermal conductivity, c_p is the specific heat at constant pressure, σ is the electrical conductivity, ρ is the density and B_0 is the uniformly applied magnetic field strength.

The initial and boundary conditions are:

$$\left. \begin{aligned} t' \leq 0 : u' = 0, T' = T'_\infty, c' = c'_\infty \quad \forall y' \\ t' \leq 0 : u' = 0, T' = T'_\infty, c' = c'_\infty \quad \forall y' \\ \frac{\partial c'}{\partial y'} = -\frac{m'_w(t)}{D} = -\frac{c'_\infty}{2\sqrt{\nu t'}} \text{ at } y' = 0 \\ u' = u'_0(1 - e^{-m_1 t'}), T' = T'_\infty, c' = c'_\infty \text{ as } y' \rightarrow \infty \end{aligned} \right\} \quad (5)$$

where $m_1 = \sigma B_0^2 / \rho$. The last boundary condition on velocity is obtained by integrating equation (2) at the boundary layer edge, where

$$\frac{\partial u'}{\partial y'} = \frac{\partial^2 u'}{\partial y'^2} = 0, \quad T' = T'_\infty, \quad c' = c'_\infty.$$

Introducing the following non-dimensional quantities:

$$y = \frac{y' u'_0}{v}, \quad t = \frac{t' u'_0{}^2}{v}, \quad u = \frac{u'}{u'_0}, \quad v = \frac{v'}{u'_0}, \quad v_w = \frac{v'_w}{u'_0}, \quad \theta = \frac{T' - T'_\infty}{T'_\infty}, \quad c = \frac{c' - c'_\infty}{c'_\infty}$$

$$Gr = \frac{v g \beta T'_\infty}{u'_0{}^3} \text{ (Grashof numbers)}, \quad m = \frac{\sigma B_0{}^2 v}{\rho u'_0{}^2} \text{ (Magnetic parameter)},$$

$$Gc = \frac{v g \beta^* c'_\infty}{u'_0{}^3} \text{ (Modified Grashof number)}, \quad Pr = \frac{\mu c_p}{\kappa} \text{ (Prandtl number)},$$

$$Sc = \frac{v}{D} \text{ (Schmidt number)}$$

and then applying the following transformations:

$$\left. \begin{aligned} u &= \sum_{i=0}^{\infty} (mt)^i f_i(\eta), \quad \theta = \theta(\eta), \quad c = c(\eta), \\ \eta &= \frac{y}{2\sqrt{t}}, \quad v_w(t) = -\frac{a}{\sqrt{t}} \end{aligned} \right\} \quad (6)$$

equations (2) and (4) are reduced to the following set of ordinary linear differential equations:

$$\theta'' + 2Pr(a + \eta)\theta' = 0, \quad (7)$$

$$c'' + 2Sc(a + \eta)c' = 0, \quad (8)$$

$$f_0'' + 2(a + \eta)f_0' = 0, \quad (9)$$

$$f_1'' + 2(a + \eta)f_1' - 4f_1 - 4f_0 + \frac{4Gr\theta}{m} + \frac{4Gc c}{m} + 4 = 0, \quad (10)$$

$$f_i'' + 2(a + \eta)f_i' - 4i.f_i - 4f_{i-1} = 0, \quad i \geq 2, \quad (11)$$

which are associated with the following initial and boundary conditions:

$$\left. \begin{aligned} \eta = 0 : \theta' &= -1, \quad c' = -1, \quad f_0 = 1, \quad f_i = 0 \quad \forall i \geq 1 \\ \eta \rightarrow \infty : \theta &= 0, \quad c = 0, \quad f_0 = 0, \quad f_1 = 1, \quad f_2 = \frac{-1}{2!}, \quad f_i = (-1)^{i-1} \frac{1}{i!}, \quad i \geq 2 \end{aligned} \right\} \quad (12)$$

where a is the suction/injection parameter. It may be noted that for suction $a > 0$, for injection $a < 0$ and for impermeable plate $a = 0$.

The homogeneous parts of the above system of differential equation admit solutions in terms of repeated integrals of the complementary error functions (See Abramowitz and Stegun [10]). For the non-homogeneous part of equation (10) the particular integrals have been obtained by the method of undetermined coefficients. The complete solutions of equation (7) to (10), satisfying boundary conditions (12) are as follows:

$$\theta(\sqrt{Pr} \xi) = \frac{1}{\sqrt{Pr}} \frac{i^0 erf_c(\sqrt{Pr} \xi)}{i^{-1} erf_c(\sqrt{Pr} a)}, \quad \xi = a + \eta, \quad (13)$$

$$C = \frac{1}{\sqrt{Sc}} \frac{i^0 erf_c(\sqrt{Sc} \xi)}{i^{-1} erf_c(\sqrt{Sc} a)}, \quad (14)$$

$$f_0(\xi) = \frac{i^0 erf_c(\xi)}{i^0 erf_c(a)}, \quad (15)$$

$$f_1(\xi) = A i^2 \operatorname{erfc}(\xi) - \frac{i^0 \operatorname{erfc}(\xi)}{i^0 \operatorname{erfc}(a)} - \frac{4Gr i^2 \operatorname{erfc}(\sqrt{Pr} \xi)}{\sqrt{Pr} m (Pr - 1) i^{-1} \operatorname{erfc}(\sqrt{Pr} a)} - \frac{4Gc i^2 \operatorname{erfc}(\sqrt{Sc} \xi)}{\sqrt{Sc} m (Sc - 1) i^{-1} \operatorname{erfc}(\sqrt{Sc} a)} + 1, \quad (16)$$

where

$$A = \frac{4Gr i^2 \operatorname{erfc}(\sqrt{Pr} a)}{m \sqrt{Pr} (Pr - 1) i^2 \operatorname{erfc}(a) i^{-1} \operatorname{erfc}(\sqrt{Pr} a)} + \frac{4Gc i^2 \operatorname{erfc}(\sqrt{Sc} a)}{m \sqrt{Sc} (Sc - 1) i^2 \operatorname{erfc}(a) i^{-1} \operatorname{erfc}(\sqrt{Sc} a)} \quad (17)$$

It may be noted that solution of equation (16) is valid when $Pr \neq 1$ and $Sc \neq 1$. In case of $Pr = 1$ and $Sc = 1$ by taking the limiting values we get

$$f_1 = C_1 i^2 \operatorname{erfc}(\xi) + D_1 \operatorname{erfc}(\xi) + 1 \quad (18)$$

where

$$\left. \begin{aligned} C_1 &= -\frac{Gr}{m} \frac{i^0 \operatorname{erfc}(a)}{i^{-1} \operatorname{erfc}(a) i^2 \operatorname{erfc}(a)} - \frac{Gc}{m} \frac{i^0 \operatorname{erfc}(a)}{i^{-1} \operatorname{erfc}(a) i^2 \operatorname{erfc}(a)}, \\ D_1 &= \frac{1}{i^{-1} \operatorname{erfc}(a)} \left[\frac{Gr + Gc}{m} \right] - \frac{1}{i^0 \operatorname{erfc}(a)}. \end{aligned} \right\} \quad (19)$$

and the function $i^n \operatorname{erfc}(\xi)$ is the repeated integral of complementary error function defined as:

$$i^n \operatorname{erfc}(\xi) = \frac{2}{\sqrt{\pi}} \int_{\xi}^{\infty} \frac{(t - \xi)^n}{n!} e^{-t^2} dt, \quad n = 0, 1, 2, \dots \quad (20)$$

$$= \sum_{K=0}^{\infty} \frac{(-1)^K \xi^K}{2^{n-K} K! \Gamma(1 + \frac{n-K}{2})} \quad (21)$$

$$\left. \begin{aligned} i^{-1} \operatorname{erfc}(\xi) &= \frac{2}{\sqrt{\pi}} e^{-\xi^2}, i^n \operatorname{erfc}(\xi) = \operatorname{erfc}(\xi), \\ \frac{\partial}{\partial \xi} i^n \operatorname{erfc}(\xi) &= -i^{n-1} \operatorname{erfc}(\xi) \end{aligned} \right\} \quad (22)$$

and the recurrence relation is

$$i^{n-2} \operatorname{erfc}(\xi) - 2\xi i^{n-1} \operatorname{erfc}(\xi) - 2n i^n \operatorname{erfc}(\xi) = 0. \quad (23)$$

It is remarked here that the analytical solutions up to first order approximation have been obtained and higher order terms may be obtained in a similar manner. As the numerical values of functions like $\operatorname{erfc}(\sqrt{Pr} a)$ for arbitrary values of Pr , Sc and parameter a are not readily available, the differential equations (7) to (11), up to second order with boundary conditions (12) have also been solved numerically on computer. For the numerical solution of (7) to (11), the unknown initial values have been computed by the method suggested by Jain and Menon [11] for linear boundary value problems. For this purpose, the Runge-Kutta-Gill integration scheme with a

step size of 0.01 has been adopted . To ensure the accuracy of the numerical results so obtained , we have compared these results with the results obtained by exact solutions in some simple cases ($a = 0$) in which the numerical values of are readily available in Abramowitz and Stegun [10] and found that the numerical results obtained by both the methods are in good agreement.

3. SKIN FRICTION COEFFICIENT

The main physical quantities of interest are skin-friction coefficient

$$C_f = \frac{\mu \left(\frac{\partial u'}{\partial y'} \right)_{y'=0}}{\rho u_0'^2 / 2} \tag{24}$$

which, in present case, can be expressed in the following form:

$$C_f = \frac{1}{\sqrt{t}} \sum_{i=0}^{\infty} (mt)^i f'_i(0) . \tag{25}$$

Numerical values of functions f'_i , $\theta(0)$ and $c(0)$ for $i = 0$ to 2 obtained by numerical solution for $m = 0.5$; $Pr = 0.72$; $a = -0.5, 0, 0.5$; $Gr = 5.0, 10.0$; $Gc = 2.0, 4.0$ and $Sc = 0.30, 0.60, 2.62$ are presented in Table 1.

Table 1. Numerical values of wall shear stress functions f'_i , $i = 0, 1, 2$, wall temperature $\theta(0)$ function and concentration function $c(0)$ for $m = 0.5$ and $Pr = 0.72$

a	Gr	Gc	Sc	$\theta(0)$	$c(0)$	$f'_0(0)$	$f'_1(0)$	$f'_2(0)$
0.5	5.0	2.0	0.30	0.68585	1.21744	-1.83271	17.2102	-3.78202
0.5	5.0	4.0	0.30	0.68585	1.21744	-1.83271	24.6409	-5.34521
0.5	10.0	2.0	0.30	0.68585	1.21744	-1.83271	25.1569	-5.08443
0.5	5.0	2.0	0.60	0.68585	0.77613	-1.83271	13.6166	-2.88563
0.5	5.0	2.0	2.62	0.68585	0.26603	-1.83271	10.4687	-2.28549
0.0	5.0	2.0	0.30	1.04443	1.61496	-1.12838	23.2893	-4.88736
-0.5	5.0	2.0	0.30	1.81493	2.25838	-0.57795	34.8856	-6.98611

Stokes [12] was the first to find an exact solution to the Navier-stokes equation for the case of flow past an impulsively started infinite horizontal plate in a viscous incompressible fluid. The Stokes problems which are of practical interest have been considered for single fluid. However, in nature, there is present a foreign mass like water vapor, carbon dioxide, helium etc. Hence we have to consider the flow of binary fluids. To study the effects of mass transfer on the flow, the value of the Schmidt number Sc is chosen to be 0.30, 0.60 and 2.62 which represent the diffusing chemical species of most common interest in air ($Pr = 0.72$), namely He , H_2O and propyl benzene, respectively (Perry [13]). The value of the magnetic field parameter m is chosen to be 0.5 in all the cases.

Figure 1 shows that the curve of skin-friction coefficient C_f increases with time and become asymptotic as t approaches 0.7. It may be observed that C_f increases with

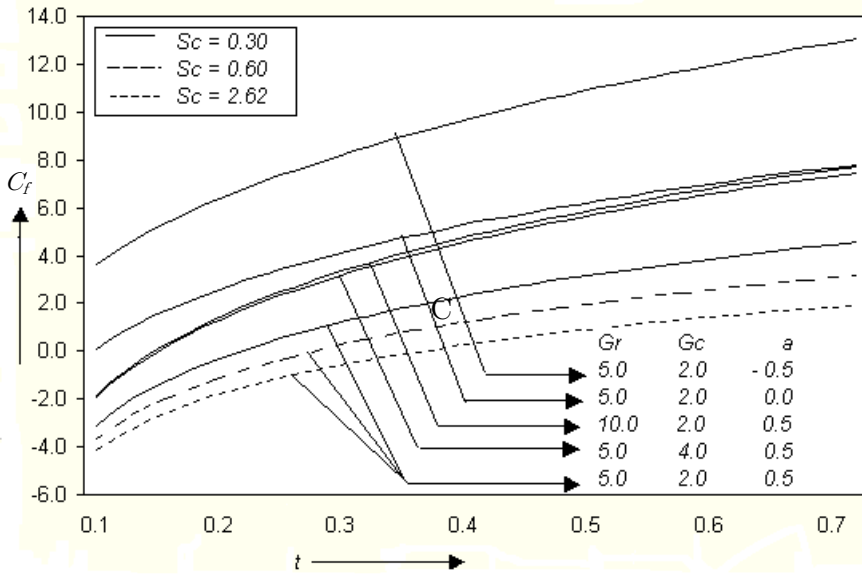


Figure 1. Variation of skin-friction coefficient with time at fixed values of $m = 0.5$ and $Pr = 0.72$

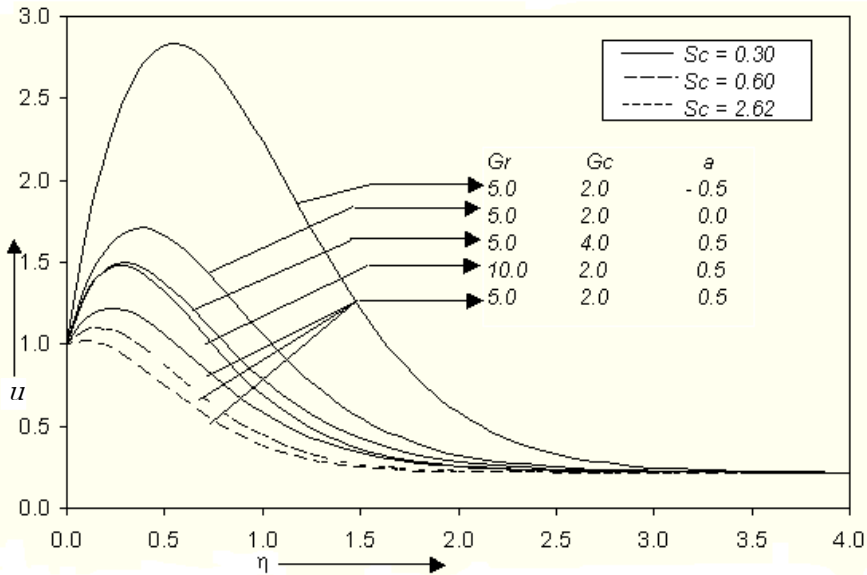


Figure 2. Velocity profile at fixed values of $t = 0.5$, $m = 0.5$ and $Pr = 0.72$

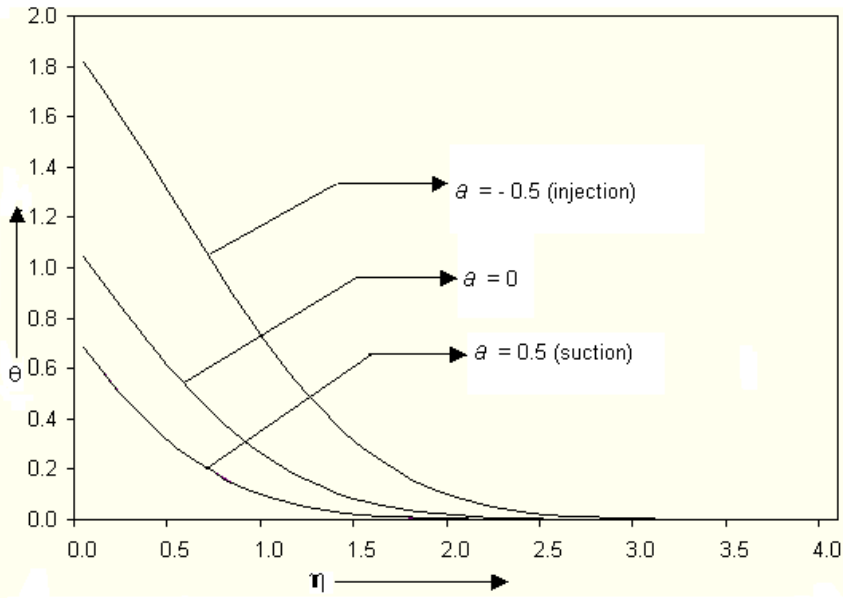


Figure 3. Temperature profile at fixed values of $t = 0.5$, $m = 0.5$ and $Pr = 0.72$

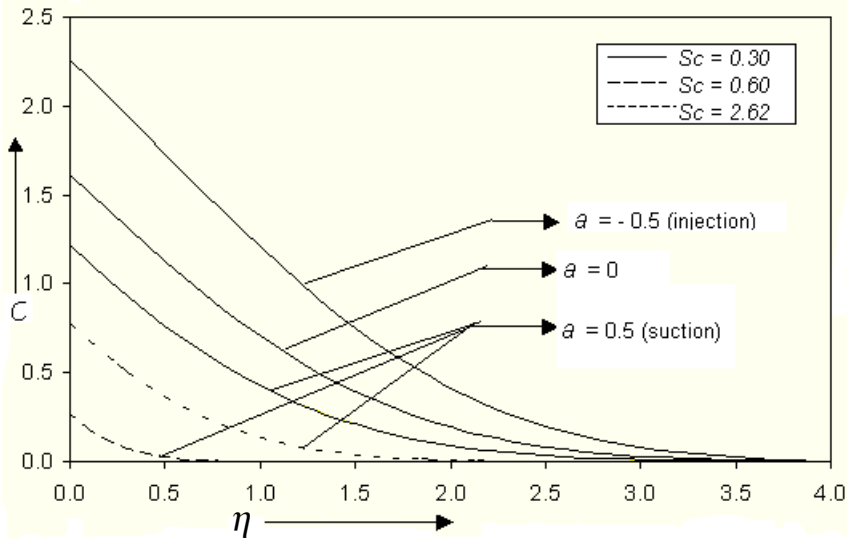


Figure 4. Concentration profile at fixed values of $t = 0.5$, $m = 0.5$ and $Pr = 0.72$

the Grashof number Gr and modified Grashof number Gc whereas it decreases as the Schmidt number Sc and the suction/injection parameter a increases. Therefore the presence of foreign species reduces the skin friction.

In Figure 2, the velocity function u is plotted against η . It is observed from the figure that the velocity decreases as a or Sc increases whereas the velocity increases with Gr or Gc for a fixed η . Thus the presence of foreign species decreases the velocity boundary layer thickness. It may also be noted that for the large value of η , the velocity u approaches 0.22 when $m = 0.5$ and $t = 0.5$ showing that the numerical solution satisfies the boundary condition 5 as $y \rightarrow \infty$ the exact value being 0.221199. This also indicates the accuracy of the numerical solutions.

In Figure 3, the temperature profiles are plotted against the variable η . It is observed that as a increases, the temperature function θ decreases for a fixed η .

In Figure 4 the concentration profiles are plotted against the variable η . It may be noted that the concentration decreases as the parameter a or Sc increases for a fixed η .

4. CONCLUSIONS

1. Since the graph of C_f becomes asymptotic for $t \geq 0.7$ in all the cases, it may be concluded that the flow is reduced to steadiness after time $t = 0.7$.
2. Presence of foreign species reduces the skin friction and velocity.
3. The thermal boundary layer thickness decreases as the suction/injection parameter a increases.
4. The concentration function decreases as the parameter a increases for a fixed value of Sc .
5. The velocity boundary layer thickness decreases as a , or increases whereas it increases with Gr or Gc .
6. While the plate moves upward with the uniform velocity, the fluid near the plate moves with greater velocity due to convection, Particularly in the case of injection of the plate.

REFERENCES

1. ELBASHBESHY, E. M. A: Heat and mass transfer along a vertical plate in the presence of magnetic field. *Indian Journal of Pure and Applied Mathematics*, **27**(6), (1996), 621-???
2. POHLHAUSEN, E: Der Wärmeaustausch zwischen festen Körpern und Flüssigkeiten mit kleiner Reibung und kleiner Wärmeleitung. *Zeitschrift für Angewandte Mathematik und Mechanik*, **1**, (1921), 115-121.
3. MOHSIN, M. A. and MANDAL, A. C.: Mass transfer effects on the unsteady hydromagnetic free convection flow past an accelerated vertical porous plate. *Journal of Physics D: Applied Physics*, 18(7), (1985), L-53.
4. DAVE, ABHA, BANSAL, J. L. and JAT, R. N.: Heat mass and momentum transfer in unsteady hydromagnetic free convection flow past an accelerated vertical plate. *Proceedings of the National Academy of Sciences, India Section A: Physical Sciences*, **50**, (1990), 211-225.

5. PATHAK, G. AND TAK, S. S.: Heat and momentum transfer in free convection flow due to hot vertical accelerated plate in presence of transverse magnetic field. *Journal of Ultra Scientist of Physical Sciences*, **14**(2), (2002), 240-247.
6. SOUNDALGEKAR, V. M.: Free convection effects on the Stokes problem for an infinite vertical plate. *Journal of Heat Transfer (ASME)*, **99**, (1977), 499-501.
7. TAK, S. S. and PATHAK, G.: Unsteady free convection along a hot vertical plate suddenly set in motion in presence of transverse magnetic field. *Far East Journal of Applied Mathematics*, **8**(3), (2002), 169-182.
8. TAK, S. S. and SISODIA, G. S.: Viscous heating in unsteady free convection along a hot vertical plate suddenly set in motion in presence of transverse magnetic field. *Proc. Int. Conf. SSFA, VOL . II*, (2002), 65-73.
9. GEBHART, B.: *Heat Transfer*. Second Edition, McGraw-Hill, 1971.
10. ABRAMOWITZ, M. and STEGUN, I. A.: *Hand Book of Mathematical Functions with Formulas, Graphs and Mathematical Tables*, Dover, Tenth Edition, 1972, p. 299.
11. JAIN, A. C. and MENON, K. R.: Görtler's series solution of laminar boundary layer equations with suction or injection. *Zeitschrift für Angewandte Mathematik und Mechanik*. **51**, (1971), 245-254.
12. STOKES, G. G.: On the effect of the internal friction of fluids on the motion of pendulums. *Proceedings of the Cambridge Philosophical Society*, **9**, (1851), 8-106.
13. Perry, J. H.: *Chemical Engineers Handbook*. 4th Edition, McGraw-Hill, 1963.

THERMOELASTIC ANALYSIS OF THICK-WALLED FUNCTIONALLY GRADED SPHERICAL PRESSURE VESSELS WITH TEMPERATURE-DEPENDENT MATERIAL PROPERTIES

DÁVID GÖNCZI

Institute of Applied Mechanics, University of Miskolc
H-3515 Miskolc-Egyetemváros
mechgoda@uni-miskolc.hu

[Received: July 19, 2017; Accepted: September 14, 2017]

Abstract. The main objective of this paper is the determination of the displacement field and the associated stresses in spherical pressure vessels made of functionally graded materials which are subjected to axisymmetric thermal and mechanical loadings. The material properties are arbitrary functions of the radial coordinate and the temperature field. A numerical solution of this steady-state thermoelastic problem is presented which is based on a multilayered approach. The developed method can be used as an analytical solution for layered composite spherical bodies. The equations of the steady-state heat conduction and field equations of thermoelasticity are used for the problem, furthermore the original problem is solved as the superposition of two subproblems with simpler loads. The results of the developed solution are checked by an analytical solution where the linear thermal expansion is a specific function of the radial coordinate and the temperature, furthermore the Young modulus depends on the radial coordinate. The numerical results for functionally graded spheres under the action of constant pressure and temperature load are compared to the results of finite element simulation.

Mathematical Subject Classification: 74B05

Keywords: FGM sphere, thermoelastic stresses, temperature-dependent, multilayered.

1. INTRODUCTION

In recent decades, laminated or layered composite and functionally graded materials (FGM) have been widely used in numerous engineering applications due to their excellent material behavior. The concept of FGM was first considered in Japan in 1984 during a hypersonic space plane project. The body of the spaceplane is exposed to a very high temperature environment (about 2000 K), with a temperature gradient of approximately 1000 K, between the inside and outside of the spaceplane. At that time there was no uniform material able to endure such conditions. In a functionally graded material the composition and structure gradually change, resulting in a corresponding change in the material properties. These advanced materials have improved thermal resistance and mechanical properties. The smooth transition between the

material properties decreases the chance of cracking and debonding under thermal and mechanical loads.

In recent years this concept has become more popular; papers and textbooks deal with the determination of thermal stresses and displacements within simple structural components (such as cylindrical and spherical vessels, disks) caused by axisymmetric steady-state temperature field and mechanical loading.

Books by Boley and Weiner [1], Lekhnitskii [2] and Lomakin [3] give solutions to many linearly elastic problem for non-homogeneous bodies. The analytical solutions for the stresses and displacements in spheres and cylinders made of functionally graded materials (radially graded) are given by Lutz and Zimmerman [4]. Their paper considered thick spherical and cylindrical bodies under radial thermal loads where the composition of the constituent materials was linear. The work by Tutuncu and Ozturk [5] derived closed-form analytical solutions for the stresses in functionally graded cylindrical and spherical bodies, subjected to internal pressure alone. Radially varying inhomogeneous material properties were considered using material stiffness which obeys a simple power-law and stress distributions depending on an inhomogeneity constant.

There are a number of works where multilayered or heterogeneous structural components are analysed, for example in [6–9]. The paper of Obata and Noda [10] studied a one-dimensional steady-state thermal stress problem for functionally graded hollow circular cylinders and hollow spheres by the use of a perturbation approach to achieve the effect of the composition on stresses and to design the optimum FGM hollow circular cylinder and hollow sphere, under different assumptions of temperature distributions. The unsteady-state thermal stress field of FG circular hollow cylinders based on a multilayered method and Green functions was presented by Kim and Noda [11].

Gönczi and Ecsedi [12] dealt with the steady-state thermoelastic problem of functionally graded disks where the material properties were arbitrary functions of the radial coordinate. Eslami et al. [13] investigated the thermal and mechanical stresses in hollow FGM spheres using a direct method to solve the heat conduction and Navier equations, while the temperature distribution was assumed to be a function of the radial coordinate.

Nayak et al. [14] developed an analytical solution to obtain the radial, tangential and effective stresses within thick spherical pressure vessels made of FGMs subjected to axisymmetric mechanical and thermal loads. The material properties of the vessel are assumed to be graded in the radial direction based on the power-law function of the radial coordinate but the Poisson ratio has constant value. A work by Bayat et al. [15] dealt with the previously presented problem too and investigates the effect of the power-law index on the stress distribution. However these papers neglect the temperature dependence of the functionally graded materials.

The FGM concept can be applied to various structural components such as to pressure vessels. This paper deals with the numerical analysis of FGM spherical pressure vessels. We consider a spherical pressure vessel made of functionally graded material which is subjected to axisymmetric thermal and mechanical loads on the

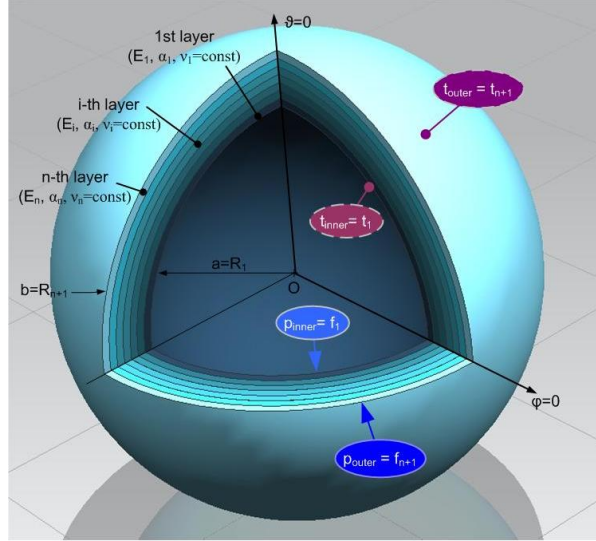


Figure 1. The multilayered model of the functionally graded sphere.

inner and outer boundary surfaces. This hollow functionally graded spherical body is subjected to unidirectional steady-state heat conduction with stress and thermal boundary conditions of the first kind on the boundary surfaces.

This paper presents a numerical method which approximates the thermoelastic problem of functionally graded spherical vessels with a problem of multilayered spherical bodies (Figure 1). The constant pressure is denoted by p_{outer} which acts on the outer curved boundary surface while the uniformly distributed mechanical loading exerted on the inner surface is denoted by p_{inner} . The radial stresses, the heat-flow and the temperature field are all continuous functions of the radial coordinate r ; furthermore the material properties are position- (radial coordinate) and temperature-dependent.

In our model the layers are made of homogeneous materials and are perfectly bonded, the material properties are constants within the layers but varying radially between them. The more layers are considered, the more accurate the computation will be (by FGMs: $n \rightarrow \infty$). Both the boundary conditions and the field equations [1, 16] are linear; therefore, the superposition principle can be used. This means that we can add the stresses and displacements caused by mechanical loads to the thermal stresses and displacements in order to solve this coupled problem. A spherical coordinate system is used to solve this problem.

2. THE FUNCTIONS OF THE MATERIAL PROPERTIES

Within the functionally graded material the volume fraction of the constituent materials gradually varies in the gradation direction, thus the effective properties of FGMs change along this direction. Since functionally graded structures are most commonly

used in high temperature environment where significant changes in mechanical properties of the constituent materials are to be expected [17,18], it is essential to take into consideration this temperature-dependency for accurate prediction of the mechanical response. Thus, the effective Young's modulus E_f , the Poisson ratio ν_f , the linear thermal expansion coefficient α_f and the thermal conductivity λ_f are assumed to be temperature dependent.

There are several methods to calculate these effective properties, such as the Mori–Tanaka scheme [19] for regions of the graded microstructure which have a well-defined continuous matrix and a discontinuous particulate phase or the self-consistent method [17], which assumes that each reinforcement inclusion is embedded in a continuum material and does not distinguish between matrix and reinforcement phases.

In many cases the effective material parameters can be expressed as nonlinear functions of the temperature field [17,20].

$$M(T) = P_0(P_{-1}T^{-1} + 1 + P_1T + P_2T^2 + P_3T^3) \quad (1)$$

In equation (1) $M(T)$ denotes the functions of the considered effective material properties (E , ν , α and λ), P_0 , P_{-1} , P_1 , P_2 and P_3 are material dependent coefficients of the absolute temperature ($T[K]$). Using these results we can present functions for the temperature- and position-dependent functionally graded material properties of FGM spherical bodies and plates [17]:

$$M_f(r, T) = [M_1(T) - M_2(T)] [K]^N + M_2(T) \quad (2a)$$

where

$$K^{Sphere}(r) = \frac{r-a}{b-a}, \quad \text{or} \quad K^{Plate}(z) = \frac{2z-h}{2h}. \quad (2b)$$

The indices 1 and 2 denote the constituent materials (mostly metal and ceramic components), a and b denote the inner and outer radii of the sphere, h is the thickness of the plate, z is the thickness coordinate and N is the volume fraction of the FGM.

3. DETERMINATION OF THE TEMPERATURE FIELD

At first we need to deal with the determination of the temperature field when the thermal conductivity is temperature- and radial coordinate-dependent $\lambda(T, r)$. We will approximate the temperature field of the functionally graded sphere for a temperature field of a multilayered spherical body with n quasihomogeneous layers whose thermal conductivities depend only on temperature. It is recommended to partition the body according to the function of the material properties.

$$R_{mi} = \frac{R_i + R_{i+1}}{2}, \quad \lambda_i(T) = \lambda(r = R_{mi}, T), \quad i = 1 \dots n. \quad (3)$$

For this case the nonlinear differential equation for the temperature field of the i -th layer $T_i(r)$ has the following form:

$$\frac{1}{r^2} \frac{d}{dr} \left[\lambda_i(T(r)) \cdot r^2 \frac{dT_i(r)}{dr} \right] = 0, \quad R_i \leq r \leq R_{i+1}, \quad i = 1, \dots, n. \quad (4)$$

Using the Kirchhoff integral transformation, this problem becomes linear

$$\theta = \int_0^{T_i} \lambda(\vartheta) d\vartheta, \quad \frac{1}{r^2} \frac{d}{dr} \left[r^2 \frac{d\theta}{dr} \right] = 0 \quad (5)$$

From the thermal boundary condition of first-kind the solution for the temperature field within the i -th layer can be derived in the following implicit form:

$$\int_{t_i}^{T_i} \lambda_i(\vartheta) d\vartheta = \int_{t_i}^{t_{i+1}} \lambda_i(\vartheta) d\vartheta \frac{R_{i+1}}{R_i - R_{i-1}} \left(\frac{R_i}{r} - 1 \right), \quad i = 1, \dots, n \quad (6)$$

We assume that the surface temperatures t_i of the adjacent layers are equal and the radial heatflow q is constant

$$t_{i+1} = T_i(R_{i+1}) = T_{i+1}(R_{i+1}), \quad i = 1, \dots, n, \quad (7)$$

$$\begin{aligned} \left[\lambda_i(T_i(r)) \frac{dT_i(r)}{dr} \right]_{r=R_{i+1}} &= q_i(R_{i+1}) = q_{i+1}(R_{i+1}) = \\ &= \left[\lambda_{i+1}(T_{i+1}(r)) \frac{dT_{i+1}(r)}{dr} \right]_{r=R_{i+1}}, \quad i = 1, \dots, n-1. \end{aligned} \quad (8)$$

After the manipulation of equations (5–8) the unknown t_i ($i = 2, \dots, n$) boundary temperatures of the layers can be calculated from the following system of equations

$$\text{const} = \int_{t_i}^{t_{i+1}} \lambda_i(\vartheta) d\vartheta \frac{R_{i+1}R_i}{R_i - R_{i-1}} \rightarrow t_i \quad i = 2, \dots, n, \quad (9)$$

moreover t_1 and $t_n + 1$ temperatures are given. In the next step, instead of using equation (6) to compute the function of the temperature we will fit a curve or curves – for example with the least squares method – to the temperature values t_i in order to make the further calculations easier especially the integrations. The approximation function has the following form:

$$T_{\text{appr}}(r) = \theta_{-2}r^{-2} + \theta_{-1}r^{-1} + \theta_0 + \theta_1r + \theta_2r^2. \quad (10)$$

In order to make the approximation more accurate more polynomial curves can be used to build the approximated temperature function. After the determination of the temperature field, the temperatures in the middle of the different layers are calculated for the approximation function of the material parameters.

$$t_{mi} = T_i(r = R_{mi}), \quad i = 1, \dots, n. \quad (11)$$

4. APPROXIMATION OF THE MATERIAL PARAMETERS

The second step is the approximation of the material properties $E(r, T(r))$, $\alpha(r, T(r))$ and $\nu(r, T(r))$ and the computation of their discrete values for the different homogeneous layers of the multilayered spherical model. We assign the following material

properties for the spherical layers according to the functions of the material parameters M :

$$L_{iv} = \left| \frac{M(a) - M(b)}{n} \right|, \quad M(a) + (i - 1)L_{iv} = M(R_i) \rightarrow R_i, \quad i = 1 \dots n + 1$$

$$E_i = E(r = R_{mi}, T = t_{mi}), \nu_i = \nu(r = R_{mi}, T = t_{mi}),$$

$$\alpha_i = \alpha(r = R_{mi}, T = t_{mi}), \quad i = 1 \dots n.$$
(12)

This means that we will approximate the arbitrary functions of the functionally graded material parameters with multisteped functions. To build the approximation function from the n step we can use for example the *Heaviside* function. Figure 2 indicates a sketch of the i -th layer for the multilayered spherical body. The constant mechanical loads exerted on the inner and outer surfaces of the i -th layer are denoted by f_i and f_{i+1} respectively. The temperatures on the boundary surfaces are t_i and t_{i+1} .

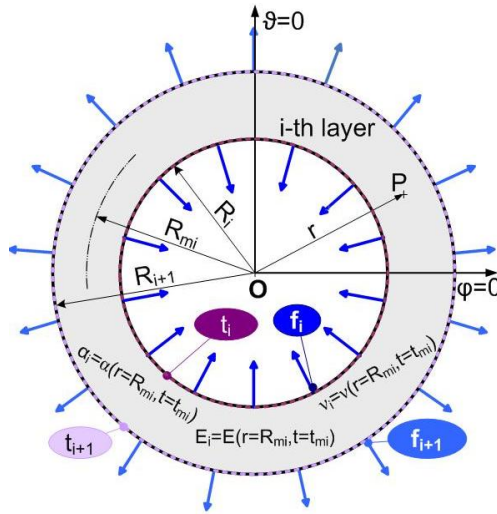


Figure 2. Sketch of the i -th layer with the mechanical and thermal loads

5. THE SOLUTION OF THE THERMOELASTIC PROBLEM

In the next step the problem will be calculated in two parts, then the principle of superposition will be used to solve the problem. In the first case the i -th layer is under thermal loading (t_i, t_{i+1}) and has the previously calculated steady-state temperature field, the stresses on the boundary surfaces ($f_i = f_{i+1} = 0$) of the layers have zero value. The thermal radial displacement $u_i^T(r)$ and the thermal stresses $\sigma_{ir}^T(r), \sigma_{i\varphi}^T(r)$,

$\sigma_{i\theta}^T(r)$ have the following forms [1]:

$$u_i^T(r) = \frac{1 + \nu_i}{1 - \nu_i} \alpha_i \left[\frac{1}{r^2} \int_{R_1}^r r^2 \tau_i(r) dr + \frac{2(1 - 2\nu_i)}{1 + \nu_i} \frac{r}{R_{i+1}^3 - R_i^3} \int_{R_1}^{R_2} r^2 \tau_i(r) dr + \frac{R_i^3}{R_{i+1}^3 - R_i^3} \frac{1}{r^2} \int_{R_1}^{R_2} r^2 \tau_i(r) dr \right], \quad (13)$$

$$\sigma_{ir}^T(r) = \frac{\alpha_i E_i}{1 - \nu_i} \left[\frac{2}{r^3} \frac{r^3 - R_i^3}{R_{i+1}^3 - R_i^3} \int_{R_1}^{R_2} r^2 \tau_i(r) dr - \frac{2}{r^3} \int_{R_1}^r r^2 \tau_i(r) dr \right], \quad (14)$$

$$\sigma_{i\phi}^T(r) = \sigma_{i\vartheta}^T(r) = \frac{\alpha_i E_i}{1 - \nu_i} \left[\frac{1}{r^3} \frac{2r^3 - R_i^3}{R_{i+1}^3 - R_i^3} \int_{R_1}^{R_2} r^2 \tau_i(r) dr - \frac{1}{r^3} \int_{R_1}^r r^2 \tau_i(r) dr - \tau_i(r) \right], \quad (15)$$

$i = 1, \dots, n,$

where $\tau_i(r)$ is the function of temperature difference of the i -th layer compared to a t_{ref} reference temperature. Because of the approximation of the temperature field, the integrals of equations (13–15) contain fourth degree polynomials ($r^2 \tau_i(r) = r^2(T_{appr} - t_{ref})$) which can be easily calculated.

6. SOLUTION OF THE ELASTICITY PROBLEM

In the second case it is assumed that the inner and outer boundary surfaces of the i -th spherical layer is under constant mechanical loading (f_i and f_{i+1}) without the thermal loads. The differential equation for the radial displacement field $u_i^M(r)$ can be derived from the equilibrium equations. The solution of this equation and the normal stresses have the following forms [1]:

$$u_i^M(r) = A_i r + \frac{B_i}{r^2}, \quad (16)$$

$$\sigma_{ir}^M(r) = 2G_i \left(\frac{1 + \nu_i}{1 - 2\nu_i} A_i - \frac{2}{r^3} B_i \right), \quad (17)$$

$$\sigma_{i\phi}^M(r) = \sigma_{i\vartheta}^M(r) = 2G_i \left(\frac{1 + \nu_i}{1 - 2\nu_i} A_i + \frac{1}{r^3} B_i \right), \quad i = 1, \dots, n.$$

The unknown parameters A_i and B_i can be determined from the equations of the boundary conditions ($\sigma_{ir}^M(R_i) = f_i, \sigma_{ir}^M(R_{i+1}) = f_{i+1}$) and we can use them to derive the expressions of the normal stresses.

$$A_i = \frac{(1 - 2\nu_i)(R_{i+1}^3 f_{i+1} - R_i^3 f_i)}{2G_i(1 + \nu_i)(R_{i+1}^3 - R_i^3)}, \quad B_i = \frac{R_{i+1}^3 R_i^3 (f_{i+1} - f_i)}{4G_i(R_{i+1}^3 - R_i^3)}, \quad (18)$$

$$\sigma_{ir}^M(r) = \frac{R_{i+1}^3 f_{i+1} - R_i^3 f_i}{R_{i+1}^3 - R_i^3} - \frac{R_{i+1}^3 R_i^3 (f_{i+1} - f_i)}{R_{i+1}^3 - R_i^3} \frac{1}{r^3}, \quad (19)$$

$$\sigma_{i\phi}^M(r) = \frac{R_{i+1}^3 f_{i+1} - R_i^3 f_i}{R_{i+1}^3 - R_i^3} - \frac{R_{i+1}^3 R_i^3 (f_i - f_{i+1})}{2(R_{i+1}^3 - R_i^3)} \frac{1}{r^3}, \quad i = 1, \dots, n. \quad (20)$$

7. THE SUPERPOSITION OF THE THERMAL AND MECHANICAL LOADS

The principle of superposition can be utilized for this problem, because both the previously used field equations and boundary conditions are linear. This means that we can add the stresses and displacements caused by mechanical loads (16–20) to the thermal stresses and displacements (13–15) in order to solve this problem. For the computation of the radial displacement and radial and tangential stresses the following equations are used:

$$\begin{aligned} u_i(r) &= u_i^T(r) + u_i^M(r), \quad \sigma_{ir}(r) = \sigma_{ir}^T(r) + \sigma_{ir}^M(r), \\ \sigma_{i\phi}(r) &= \sigma_{i\phi}^T(r) + \sigma_{i\phi}^M(r), \quad i = 1, \dots, n. \end{aligned} \quad (21)$$

The unknown parameters $f_i (i = 2, \dots, n)$ in the equations of $u_i^M(r)$, $\sigma_{ir}^M(r)$, $\sigma_{i\phi}^M(r)$ can be calculated from the following equations

$$u_i(R_{i+1}) = u_{i+1}(R_{i+1}), \quad i = 1, \dots, n-1, \quad (22)$$

which ensure the continuity of the radial displacement field and furthermore f_1 and f_{n+1} are given.

$$\sigma_{1r}(R_1) = f_1 = -p_1, \quad \sigma_{nr}(R_{n+1}) = f_{n+1} = -p_{n+1}. \quad (23)$$

The system of equations (20) has the following form:

$$a_i f_i + b_i f_{i+1} + c_i f_{i+2} = u_{i+1}^T(R_{i+1}) - u_i^T(R_{i+1}), \quad i = 2, \dots, n-1. \quad (24)$$

where the constants a_i , b_i and c_i are

$$a_i = \frac{3R_i^3 R_{i+1}}{4G_i(R_{i+1}^3 - R_i^3)} \frac{(1 - \nu_i)}{(1 + \nu_i)}, \quad (25)$$

$$\begin{aligned} b_i &= -\frac{R_{i+1}}{2G_{i+1}(R_{i+2}^3 - R_{i+1}^3)} \left[\frac{(1 - 2\nu_{i+1})}{(1 + \nu_{i+1})} R_{i+1}^3 + \frac{R_{i+3}^3}{2} \right] - \\ &\quad - \frac{R_{i+1}}{2G_i(R_{i+1}^3 - R_i^3)} \left[\frac{(1 - 2\nu_i)}{(1 + \nu_i)} R_{i+1}^3 + \frac{R_i^3}{2} \right], \end{aligned} \quad (26)$$

$$c_i = \frac{3R_{i+2}^3 R_{i+1}}{4G_{i+1}(R_{i+2}^3 - R_{i+1}^3)} \frac{(1 - \nu_{i+1})}{(1 + \nu_{i+1})}, \quad i = 2, \dots, n-1. \quad (27)$$

Using the previously determined parameters f_i and equation (21) the radial displacement and the normal stresses of the multilayered spherical body can be evaluated. Due to the multilayered model the curve of the tangential normal stress may contain significant steps, but the stress values in the middle of each layer have good accuracy. Thus an approximate curve can be fitted to these points to increase the accuracy and convergence of the method. The recommended form of the approximate curve when $15 > N > 0.15$:

$$\sigma_{\phi-approx}(r) = F_{-3}r^{-3} + F_{-2}r^{-2} + F_{-1}r^{-1} + F_0 + F_1r + F_2r^2. \quad (28)$$

8. AN ANALYTICAL SOLUTION

An analytical solution is developed for the case when the Poisson ratio is constant, the distribution of the Young modulus is assumed to be described with a power-law along the radial coordinate [1], [15] the linear thermal expansion specifically depends on the temperature and radial coordinate, furthermore the temperature field has special form:

$$E(r) = P_1 \left(\frac{r}{a}\right)^{m_E}, \quad \alpha(r, T(r)) = (P_2 + P_3 T(r)) \left(\frac{r}{a}\right)^{m_\alpha}, \quad (29)$$

$$T(r) = H_1 - \frac{H_2}{r}, \quad \text{if } \lambda = \text{const.} : \quad (30)$$

$$H_1 = t_{inner} - (t_{outer} - t_{inner}) \frac{b}{a-b}, \quad H_2 = (t_{outer} - t_{inner}) \frac{ab}{a-b},$$

where P_1, P_2, P_3, m_E and m_α are material parameters. The strain-displacement and the stress-strain relations for spherical bodies can be expressed as [1], [16]:

$$\varepsilon_r = \frac{du}{dr}, \quad \varepsilon_\phi = \frac{u}{r}, \quad (31)$$

$$\sigma_r(r) = \frac{E}{(1-2\nu)(1+\nu)} [(1-\nu)\varepsilon_r + 2\nu\varepsilon_\phi - \alpha(1+\nu)T], \quad (32)$$

$$\sigma_\theta(r) = \sigma_\phi(r) = \frac{E}{(1-2\nu)(1+\nu)} [\nu\varepsilon_r + \varepsilon_\phi - \alpha(1+\nu)T]. \quad (33)$$

In this case the differential equation derived from the equilibrium equation for the radial displacement is

$$(1-\nu) \frac{d^2 u}{dr^2} + (m_E + 2) \frac{(1-\nu)}{r} \frac{du}{dr} + 2[\nu(m_E + 1) - 1] \frac{u}{r^2} = A_1 r^{m_\alpha - 1} + A_2 r^{m_\alpha - 2} + A_3 r^{m_\alpha - 3}, \quad (34)$$

where the constants A_1, A_2 and A_3 are

$$A_1 = \frac{1+\nu}{a^{m_\alpha}} (-m_E - m_\alpha) H_1 (P_2 + P_3 H_1), \quad (35)$$

$$A_2 = \frac{1+\nu}{a^{m_\alpha}} (m_E + m_\alpha - 1) H_2 (P_2 + 2P_3 H_1), \quad (36)$$

$$A_3 = \frac{1+\nu}{a^{m_\alpha}} (-m_E - m_\alpha + 2) P_3 H_2^2. \quad (37)$$

The solution of the (34) differential equation:

$$u(r) = C_1 r^{\lambda_1} + C_2 r^{\lambda_2} + \frac{G_1 r^{m_\alpha + 1} + G_2 r^{m_\alpha} + G_3 r^{m_\alpha - 1}}{G_4}, \quad (38)$$

where C_1 and C_2 are unknown constants of integration and

$$\lambda_1 = \frac{1}{2} \left(-(m_E + 1) + \sqrt{m_E^2 + 9 + 2m_E \frac{1 - 6\nu + 5\nu^2}{(\nu - 1)^2}} \right), \quad (39)$$

$$\lambda_2 = \frac{1}{2} \left(-(m_E + 1) - \sqrt{m_E^2 + 9 + 2m_E \frac{1 - 6\nu + 5\nu^2}{(\nu - 1)^2}} \right), \quad (40)$$

$$G_1 = A_1 \{ 2\nu [\nu(m_E(3m_E + 5) + 2) - m_E(m_E + 6) - 4] + m_\alpha^3(\nu - 1)^2(2m_E + m_\alpha) + 2(m_E + 2) + m_\alpha(\nu - 1)[m_\alpha(m_E(1 - m_E) + 5 + \nu(m_E(m_E - 5) - 5) - m_E(5\nu(m_E + 1) - 5 - m_E))] \}, \quad (41)$$

$$G_2 = A_2 \{ m_\alpha^3(\nu - 1)^2(m_\alpha + 2m_E + 2) + m_E [m_E(2\nu - 1) - 2] + m_E\nu^2(3m_E + 2) + m_\alpha(\nu - 1)[-4m_E(m_E + 1) + m_\alpha(\nu(m_E(m_E - 2) - 5) - m_E(m_E + 2) + 5))] \}, \quad (42)$$

$$G_3 = A_3 \{ m_\alpha^3(\nu - 1)^2(m_\alpha + 2m_E + 4) + 2m_E [\nu^2(m_E + 1) + m_E\nu - 1] + m_\alpha(\nu - 1) \cdot [m_\alpha(\nu(m_E + m_E^2 + 1) - m_E^2 - 5m_E - 1) - (\nu(m_E + 1)(3m_E + 6) - m_E + m_E^2 - 6)] \}, \quad (43)$$

$$G_4 = [m_\alpha(\nu - 1)(m_\alpha + m_E + 3) - m_E(\nu + 1)] [(\nu - 1)(m_\alpha(m_\alpha + m_E - 1) - 2) + m_E(1 - 3\nu)] [(\nu - 1)(m_\alpha(m_\alpha + m_E + 1) - 2) - 2m_E\nu]. \quad (44)$$

Then the radial stress has the following form:

$$\sigma_r(r) = C_1 S_1 r^{\lambda_1 + m_E - 1} + C_2 S_2 r^{\lambda_2 + m_E - 1} + S_0 r^{m_\alpha + m_E} + S_{-1} r^{m_\alpha + m_E - 1} + S_{-2} r^{m_\alpha + m_E - 2}, \quad (45)$$

where

$$S_1 = Z [(1 - \nu)\lambda_1 + 2\nu], \quad S_2 = Z [(1 - \nu)\lambda_2 + 2\nu], \quad Z = \frac{P_1}{a^{m_E}(1 - 2\nu)(1 + \nu)}, \quad (46)$$

$$S_0 = Z \left\{ \frac{G_1}{G_4} [(1 - \nu)(m_\alpha + 1) + 2\nu] - \frac{H_1(1 + \nu)(P_2 + P_3 H_1)}{a^{m_\alpha}} \right\}, \quad (47)$$

$$S_{-1} = Z \left\{ \frac{G_2}{G_4} [(1 - \nu)m_\alpha + 2\nu] + \frac{H_2(1 + \nu)(P_2 + 2P_3 H_1)}{a^{m_\alpha}} \right\}, \quad (48)$$

$$S_{-2} = Z \left\{ \frac{G_3}{G_4} [(1 - \nu)(m_\alpha - 1) + 2\nu] - \frac{H_2^2(1 + \nu)P_3}{a^{m_\alpha}} \right\}, \quad (49)$$

The unknown constants C_1, C_2 can be obtained from the stress boundary conditions:

$$\sigma_r(a) = -p_{inner}, \quad \sigma_r(b) = -p_{outer}, \quad (50)$$

$$C_1 = \frac{b^{\lambda_2 + m_E - 1} c_a - a^{\lambda_2 + m_E - 1} c_b}{S_1 (a^{\lambda_2 + m_E - 1} b^{\lambda_1 + m_E - 1} - a^{\lambda_1 + m_E - 1} b^{\lambda_2 + m_E - 1})}, \quad (51)$$

$$C_2 = \frac{a^{\lambda_1 + m_E - 1} c_b - b^{\lambda_1 + m_E - 1} c_a}{S_2 (a^{\lambda_2 + m_E - 1} b^{\lambda_1 + m_E - 1} - a^{\lambda_1 + m_E - 1} b^{\lambda_2 + m_E - 1})},$$

$$c_a = a^{m_\alpha + m_E} (S_0 + S_{-1} a^{-1} + S_{-2} a^{-2}) + p_{inner}, \quad (52)$$

$$c_b = b^{m_\alpha + m_E} (S_0 + S_{-1} b^{-1} + S_{-2} b^{-2}) + p_{outer}.$$

9. ANALYTICAL SOLUTION FOR THE TEMPERATURE FIELD

An analytical solution is derived to check the accuracy of the method that calculates the temperature field (Section 2). The thermal conductivity is temperature- and coordinate-dependent and has the following special form:

$$\lambda(r, T(r)) = P_1 e^{P_2 T(r)} \left(\frac{r}{a} \right)^{m_\lambda}, \quad (53)$$

where P_1 , P_2 and m_λ are material constants. After solving equation (4) the temperature field can be calculated and its constants can be evaluated from the first-kind thermal boundary conditions:

$$T(r) = \frac{1}{P_2} \ln \left(\frac{P_2 C_1}{(m_\lambda + 1)} \frac{r^{-m_\lambda - 1}}{a^{-m_\lambda}} - P_2 C_1 C_2 \right), \quad (54)$$

$$C_1 = \frac{ab(m+1)(e^{t_{outer}P_2} - e^{t_{inner}P_2})}{P_2 \left(a \left(\frac{b}{a} \right)^{-m_\lambda} - b \right)}, \quad C_2 = \frac{be^{t_{outer}P_2} - ae^{t_{inner}P_2} \left(\frac{b}{a} \right)^{-m_\lambda}}{a(m+1)(e^{t_{outer}P_2} - e^{t_{inner}P_2})b}. \quad (55)$$

10. NUMERICAL EXAMPLES

This part of the paper deals with the verification of the developed methods. We used the equations of the previously presented analytical solutions and finite element simulation to verify the developed solutions. Furthermore, Maple 15 mathematical software was used to create the program of the developed method. In the first numerical example the accuracy of the calculation for the temperature field is investigated. The following data were used for equation (22) to carry out the numerical computation:

$$a = 0.04\text{m}, b = 0.06\text{m}, P_1 = 10 \frac{\text{W}}{\text{mK}}, P_2 = 1.34 \cdot 10^{-3} \frac{1}{\text{K}}, m_\lambda = 1.9,$$

$$t_{ref} = 273\text{K}, t_{inner} = 303\text{K}, t_{outer} = 623\text{K}$$

and the approximation function of the temperature field is built from two curves:

$$T_{appr}(r) = \left[Heaviside(r-a) - Heaviside \left(r - \frac{a+b}{2} \right) \right] T_{appr,1} \\ + \left[Heaviside \left(r - \frac{a+b}{2} \right) - Heaviside(r-b) \right] T_{appr,2}$$

where $T_{appr,1}$ and $T_{appr,2}$ have the forms according to equation (10); furthermore, three cases with three different layer numbers ($n_1 = 5, n_2 = 9, n_3 = 17$) are compared to the analytical solution of Eq. (54-55). Figure 3 shows the temperature function and the relative errors of the approximations when

$$e_M(\%) = \left| \frac{M_{analytical} - M_{numerical}}{M_{analytical}} \right| \cdot 100, \quad M(r) = T(r), u(r), \sigma_r(r), \sigma_\phi(r). \quad (56)$$

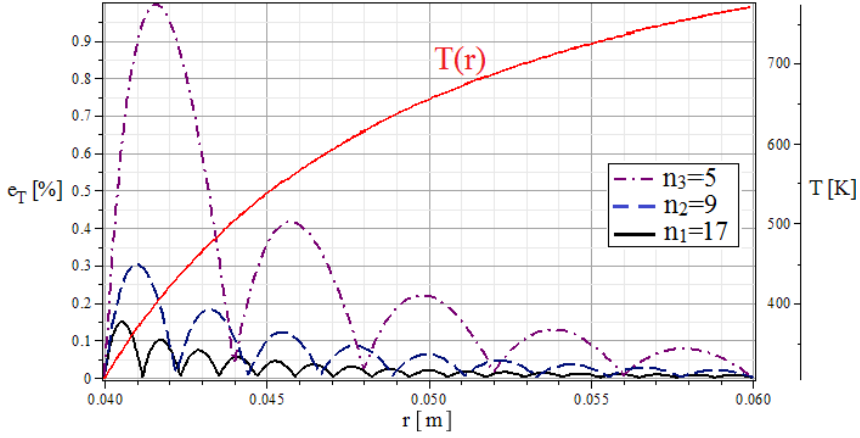


Figure 3. The temperature field and the relative errors of the model

In the second example the developed numerical method is compared to the analytical method of Section 8. The following numerical data were used to check the accuracy of the presented method:

$$a = 0.065m, b = 0.08m, P_1 = 200GPa, P_2 = 10^{-8} \frac{1}{K^2}, P_3 = 2 \cdot 10^{-8} \frac{1}{K}, m_\alpha = 1.9,$$

$$m_E = 2, \lambda = 58 \frac{W}{mK}, t_{inner} = 723K, t_{outer} = 298K, t_{ref} = 273K,$$

$$p_{inner} = 20MPa, p_{outer} = 0MPa.$$

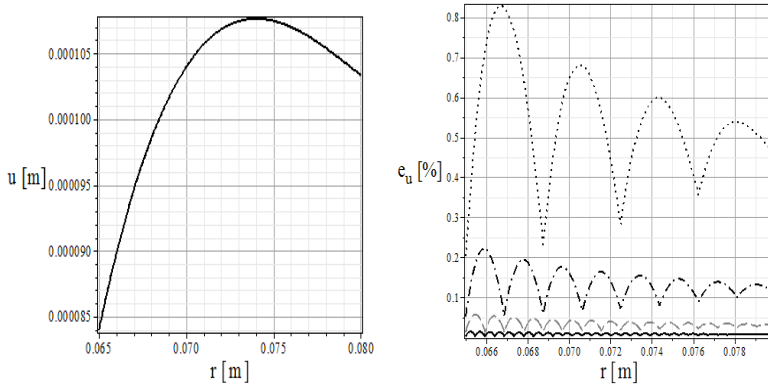


Figure 4. The radial displacement field and the relative errors ($n_1 = 4$: dots, $n_2 = 8$: dash-dot line, $n_3 = 16$: dashed line, $n_4 = 32$: solid line)

Figures (4–6) illustrate the radial displacement field, radial and tangential normal stresses, the convergence of the developed method and the relative errors $e_u(r)$, $e_{\sigma r}(r)$, $e_{\sigma \varphi}(r)$ of the numerical model compared to the analytical solution. Four different layer

numbers were used to build up the multilayered models: $n_1 = 4, n_2 = 8, n_3 = 16$ and $n_4 = 32$. Figure 6 shows the advantage of the approximation – solid continuous line – for the tangential stresses over the summarized – discontinuous line – curve.

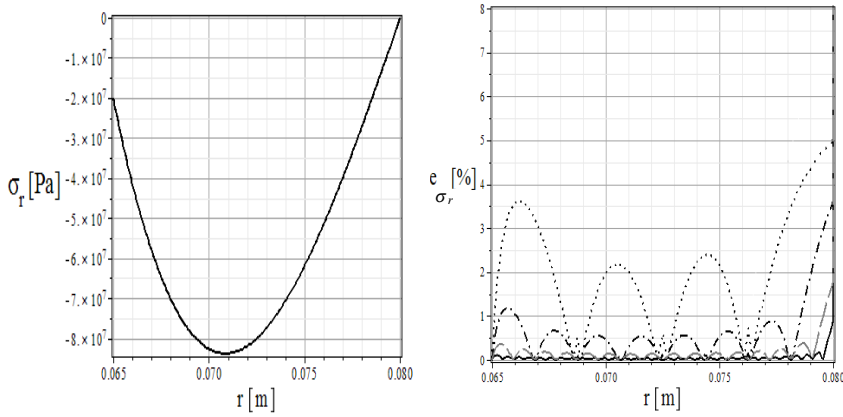


Figure 5. The radial normal stress and the relative errors ($n_1 = 4$: dots, $n_2 = 8$: dash-dot line, $n_3 = 16$: dashed line, $n_4 = 32$: solid line)

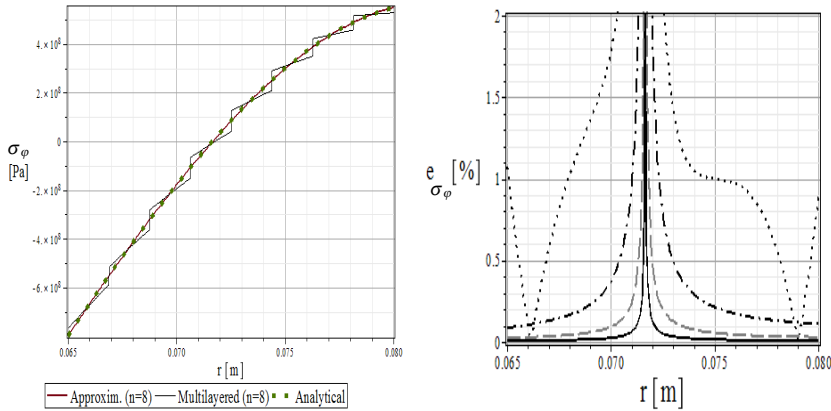


Figure 6. The tangential stress and the relative errors ($n_1 = 4$: dots, $n_2 = 8$: dash-dot line, $n_3 = 16$: dashed line, $n_4 = 32$: solid line)

In the next example a functionally graded spherical vessel is considered which is made from a steel-silicon nitride FGM and the effective material properties can be calculated by equations (1–2). In this case the results of the multilayered method are verified by finite element simulation. The finite element model was created using a commercial FE code, ABAQUS CAE. In the FEM model – due to symmetry – only

a quarter of the spherical body is created. The variation of the material properties was implemented by considering 30 layers with temperature-dependent material properties ($M_i = M(r = r_i, T(r)), i = 1, \dots, 30$). An 8-node temperature-displacement, quadrilateral element was used to mesh the vessel, the number of elements is 4201.

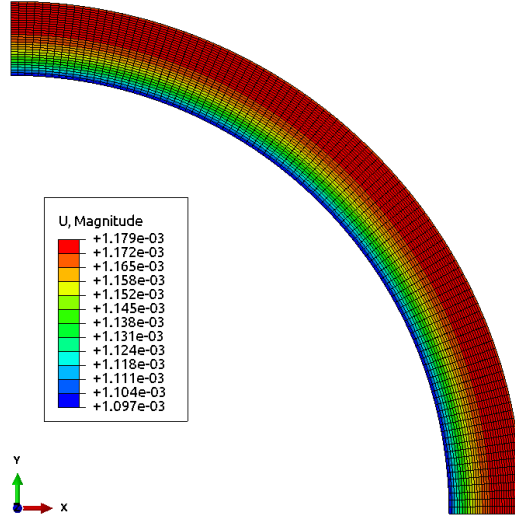


Figure 7. The finite element model and the displacement field

Figure 7 shows the mesh of the model on the deformed geometry with the displacement field. The material parameters [17], [18] can be found in Table 1, the geometry and the loads are:

$$a = 0.5\text{m}, b = 0.59\text{m}, t_{inner} = 733\text{K}, t_{outer} = 303\text{K}, t_{ref} = 273\text{K},$$

$$p_{inner} = 90\text{MPa}, p_{outer} = 0\text{MPa}.$$

Table 1. Material properties for the numerical example

material property (P)	metal (stainless steel)				ceramic (silicon nitride)			
	P_{m0}	$P_{m1}(10^{-3})$	$P_{m2}(10^{-3})$	$P_{m3}(10^{-3})$	P_{c0}	$P_{c1}(10^{-3})$	$P_{c2}(10^{-3})$	$P_{c3}(10^{-3})$
$\lambda(\text{W/mK})$	15.39	-1.264	20.92	-7.223	12.723	-1.032	5.466	-7.876
$\alpha(1/\text{K})$	$12.33 \cdot 10^6$	0.8086	0	0	$3.873 \cdot 10^6$	0.9095	0	0
$E(\text{Pa})$	$2.01 \cdot 10^{11}$	0.3079	-6.5340	0	$3.484 \cdot 10^{11}$	-0.307	2.16	-8.946
ν'	0.3262	-0.1	3.797	0	0.24	0	0	0

Table 2 contains the results of the finite element simulation and the multilayered method when the volume fraction is $N = 3$. In these case we note that if the temperature dependency of the material parameters is neglected, the relative errors are significant (for example if $M = M(r, T = 298\text{K}) = M(r)$, then the maximum error is 200MPa).

Table 2. Results of the developed method (ML) and the FE simulations

$N = 3$ $r(\text{mm})$	method	$T(r)[\text{K}]$		$u(r)[\text{mm}]$		$-\sigma_r[\text{MPa}]$		$-\sigma_\varphi[\text{MPa}]$	
		$n = 30$	$n = 180$	$n = 30$	$n = 180$	$n = 30$	$n = 180$	$n = 30$	$n = 180$
500	ML	733	733	1.09865	1.09869	90	90	-330.17	330.23
	FE	733		1.09741		90.1645		-332.17	
518.04	ML	611.750	611.751	1.14211	1.14215	93.5435	93.5468	22.0908	22.142
	FE	612.041		1.14084		98.8303		19.650	
536.07	ML	510.297	510.297	1.16493	1.16497	78.1207	78.1263	233.905	233.923
	FE	510.604		1.16352		78.3125		222.61	
554.08	ML	426.717	426.718	1.17632	1.17636	54.3166	54.3210	341.202	341.216
	FE	420.026		1.17497		54.5826		325.583	
572.08	ML	358.392	358.393	1.17974	1.17977	27.7325	27.7378	405.913	405.937
	FE	358.703		1.17846		28.0633		389.203	
590	ML	303	303	1.17159	1.17161	$7.6 \cdot 10^{-7}$	$4.3 \cdot 10^{-8}$	465.324	465.262
	FE	303		1.17049		$4.8 \cdot 10^{-4}$		476.651	

In Figures (8–10) the normalized curves of the radial displacement, radial and tangential stresses can be seen by 5 different volume fractions ($N = 0.16, 0.3, 1, 3, 6$).

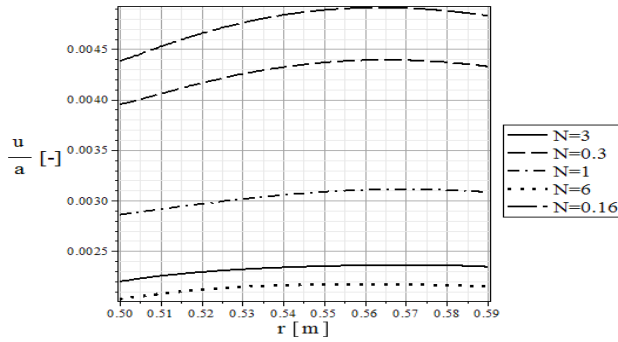


Figure 8. The normalized radial displacements by different volume fractions

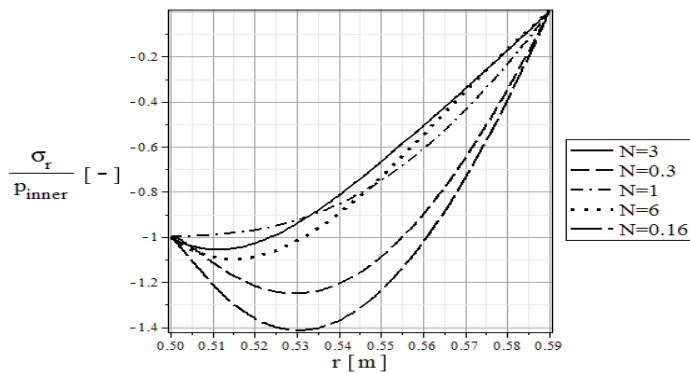


Figure 9. The normalized radial stresses by different volume fractions

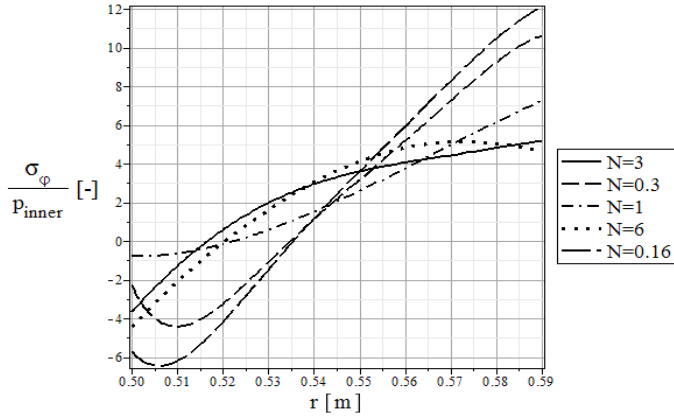


Figure 10. The normalized tangential stresses by different volume fractions.

11. CONCLUSIONS

The main objective of this paper has been to presents a numerical solution for the determination of the displacement field and normal stresses in functionally graded hollow spheres subjected to spherically symmetric thermal and mechanical loads. The material properties of the FGM are arbitrary functions of the radial coordinate and the temperature field. In the developed method the radially graded spherical pressure vessel has been modeled as a multilayered spherical body, furthermore Fourier's law of heat conduction and the equations of thermal stresses with steady-state temperature field have been used. Analytical solutions have been derived to check the accuracy of the method and the results have been compared to finite element simulations. The developed method can be utilized during the designing of the material composition along the radial coordinate for FGM spherical pressure vessels or as benchmark solutions to verify the accuracy of other numerical methods.

REFERENCES

1. BOLEY, B. A. and WEINER, J. H.: *Theory of Thermal Stresses*. John Wiley & Sons Inc., New York, 1960.
2. LEKHNITSKII, S. G.: *Theory of Elasticity of an Anisotropic Body*. Mir Publishers, Moscow, 1981.
3. LOMAKIN, V. A.: *Theory of Nonhomogeneous Elastic Bodies*. MGU, Moscow, 1976.
4. LUTZ, M. P. and ZIMMERMAN, R.W.: Thermal stresses and effective thermal expansion coefficient of a functionally graded sphere. *Journal of Thermal Stresses*, **19**, (1996), 39-54.
5. TUTUNCU, N. and OZTURK, M.: Exact solutions for stresses in functionally graded pressure vessels. *Composites, Part B*, **32**, (2001), 683-686.

6. LENGYEL, Á. J. and ECSEDI, I.: Static and dynamic analyses of composite beams with interlayer slip. *Journal of Computational and Applied Mechanics*, **10**(1), (2015), 25-40.
7. KISS, L. P. and SZEIDL, GY: Vibrations of pinned-fixed heterogeneous circular beams pre-loaded by a vertical force at the crown point. *Journal of Sounds and Vibrations*, **393C**,(2017), 92-113.
8. KISS, L. P.: Green's functions for nonhomogeneous curved beams with application to vibration problems. *Journal of Computational and Applied Mechanics*, **12**(1), (2017), 21-43.
9. LENGYEL, Á. J. and ECSEDI, I.: An analytical solution for two-layered composite beams with imperfect shear interaction. *International Review of Mechanical Engineering*, **10**(7), (2016), 508-517.
10. OBATA, Y. and NODA, N.: Steady thermal stress in a hollow circular cylinder and a hollow sphere of a functionally gradient materials. *Journal of Thermal Stresses*, **7**, (1994), 471-487.
11. KIM, K.S. and NODA, N.: Green's function approach to unsteady thermal stresses in an infinite hollow cylinder of functionally graded material. *Acta Mechanica*, **156**, (2002), 61-145.
12. GÖNCZI, D. and ECSEDI, I.: Thermoelastic analysis of functionally graded hollow circular disk. *Archieve of Mechanical Engineering*, **62**(1), (2015), 5-18.
13. ESLAMI, M. R., BABAEI, M. H. and POULTANGARI, R.: Thermal and mechanical stresses in a FG thick sphere. *International Journal of Pressure Vessels and Piping*, **82**, (2005), 522-527.
14. NAYAK, P., MONDAL, S. C. and NANDI A.: Stress, strain and displacement of a functionally graded thick spherical vessel. *International Journal of Engineering Science and Technology*, **3**(4), (2011), 2660-2671.
15. BAYAT, Y., GHANNAD, M. and TORABI, H.: Analytical and numerical analysis for the FGM thick sphere under combined pressure and temperature loading. *Archive of Applied Mechanics*, **10**, (2011), 229-242.
16. NOWINSKI, I.L.: *Theory of Thermoelasticity with Applications*. Sythoff and Noordhoff, Alpen aan den Rijn, 1978.
17. SHEN, H. S.: *Functionally Graded Materials: Nonlinear Analysis of Plates and Shells*. CRC Press, London, 2009.
18. REDDY, J. N. and CHIN, C. D.: Thermomechanical analysis of functionally graded cylinders and plates. *Journal of Thermal Stresses*, **21**, (1998), 593-626.
19. MORI, T. and TANAKA, K.: Average stress in matrix and average elastic energy of materials with misfitting inclusions, *Acta Metallurgica*, **21**, (1973), 568-582.
20. TOULOUKIAN, Y. S., GERRITSEN, J.K. and MOORE, N. Y.: *Thermophysical Properties Research Literature Retrieval Guide*. Springer, 1967.

ANALYSIS OF CONVECTIVE-RADIATIVE POROUS FIN WITH TEMPERATURE-DEPENDENT INTERNAL HEAT GENERATION AND MAGNETIC FIELD USING HOMOTOPY PERTURBATION METHOD

GBEMINIYI SOBAMOWO

Department of Mechanical Engineering, University of Lagos, Akoka, Lagos, Nigeria
mikegbeminiyi@gmail.com

OLUROTIMI ADELEYE

Department of System Engineering, University of Lagos, Akoka, Lagos, Nigeria
rotimiadeleye1711@gmail.com

AHMED YINUSA

Department of Mechanical Engineering, University of Lagos, Akoka, Lagos, Nigeria
mynotebook2010@yahoo.com

[Received: September 1, 2017; Accepted: November 15, 2017]

Abstract. In this work, thermal behavior of convective-radiative porous fin with temperature-dependent internal heat generation subjected to magnetic field using homotopy perturbation method is analyzed. The developed symbolic heat transfer model is used to investigate the effects of convective, radiative, magnetic parameters on the thermal performance of the porous fin. From the study, it is established that increase in porosity, convective, radiative and magnetic parameters increase the rate of heat transfer from the fin and consequently, improve the efficiency of the fin. The homotopy perturbation method used in the work is validated with the results of a numerical method. The results of the two methods are in excellent agreement. Therefore, this study provides a platform for comparison of results of any other method of analysis of the problem. Also, such an analytical tool is valuable as a design and optimization approach for finned heat exchangers where each fin/row is analytically analyzed and where the surrounding fluid is influenced by a magnetic field.

Mathematical Subject Classification: 05C38, 15A15

Keywords: Thermal analysis, porous fin, convective-radiative fin, magnetic field, homotopy perturbation method

1. INTRODUCTION

The continuous demands for high performance thermal equipment have been part of the driving forces behind the present advancements in thermal technology. However, the production of excess heat is inevitable during the operation of thermal equipment. If such generated excessive heat levels are not controlled or dissipated, it leads to thermal-induced failure in the thermal systems. Consequently, the need for fins or

extended surfaces as heat transfer enhancers in the thermal systems is indispensable. The applications of the extended surfaces in various systems such as electronic and microelectronics components, high-power semi-conductor devices, high-power lasers, light emitting diodes (LEDs), computer cooling, sensitive devices etc. have attracted various research interests in past decades. Also, the enhancement of heat transfer from thermal equipment and component through the use of porous fin has been a subject of research in recent times following the pioneer work of Kiwan and Al-Nimr [1]. In their analysis, the developed nonlinear model was solved numerically while Kiwan [2–4] developed a simple method to study the performance of porous fins in a natural convection environment. Also, Gorla and Bakier [5] used a numerical approach to study the thermal performance of a convective-radiative rectangular porous fin. Kundu and Bhanja [6] and Kundu et al. [7] presented an analytical model for the optimization of porous fins and computation of maximum heat transfer in porous fins. With the help of a finite difference scheme, Taklifi et al. [8] investigated the effects of magnetohydrodynamics (MHD) on the performance of a rectangular porous fin. Bhanja and Kundu [9] and Kundu et al. [10] applied Adomian decomposition method to analytically investigate thermal analysis of a constructal T-shape porous fin with radiation effects and to analyze the optimum design of porous fin of various profiles operating in convection environment, respectively. In another work, Gorla et al. [11] applied Spectral collocation method (SCM) to study the effects of variable thermal conductivity on the natural convection and radiation in porous fin. Saedodin and Shahababaei [12] adopted the homotopy perturbation method (HPM) to analyze heat transfer in longitudinal porous fins while Darvishi et al. [13] and Moradi et al. [14] and Ha et al. [15] utilized homotopy analysis method (HAM) to provide solutions to the natural convection and radiation in a porous and porous moving fins. Also, Hoshyar et al. [16] used the homotopy perturbation method and collocation method (CM) and presented thermal performance analysis of porous fins with temperature-dependent heat generation. The least square method (LSM) was used by Hatami and Ganji [17,18] to study the thermal behaviour of convective-radiative in porous fin with different sections and ceramic materials. Recently, Rostamiyaan et al. [19] applied the variational iterative method (VIM) to develop analytical solution for heat transfer in porous fins while Ghasemi et al. [20] used differential transformation method (DTM) for heat transfer analysis in porous and solid fin.

The previous research works on the thermal analysis of fin have been generally carried out using ADM, HAM, VIM, DTM etc. However, the determination of Adomian polynomials as carried out in ADM, the need for small perturbation parameter as required in traditional PMs, and the rigour of the derivations of differential transformations or recursive relation as carried out in DTM have limited the applications of these method to wider varieties of applications. Moreover, the lack of rigorous theories or proper guidance for choosing initial approximation, auxiliary linear operators, auxiliary functions, auxiliary parameters, and the requirements of conformity of the solution to the rule of coefficient ergodicity as done in HAM, the search Lagrange multiplier as carried in VIM, and the challenges associated with proper construction of the approximating functions for arbitrary domains or geometry of interest as in the Galerkin weighted residual method (GWRM), least square method (LSM)

and collocation method (CM) are some of the difficulties in the method that are not experienced by HPM. Furthermore, in the class of the newly developed approximate analytical methods, the homotopy perturbation method is considered to be relatively simple with fewer requirements for mathematical rigour or skill. It is a total approximate analytic method unlike DTM, HAM, ADM, VIM etc. where the search for a particular value that will satisfy second the boundary condition necessitates use of a numerical method with the use of a software which could result in additional computational cost in the generation of solution to the problem. Also, the homotopy perturbation method eliminates the “the small parameter assumption” as carried in the traditional perturbation methods. It is a powerful method that gives acceptable analytical results with convenient convergence and stability [21–25]. Therefore, in finding approximate analytical solutions to linear and nonlinear differential equations, HPM has fast gained ground and it appears in many engineering and scientific research papers. It is an approximate analytical method that could solve differential equations, difference equation, differential-difference equations, fractional differential equation, pantograph equation and integro-differential equation. It solves nonlinear integral and differential equations without linearization, discretization, closure, restrictive assumptions, perturbation, approximations, round-off error and discretization that could result in massive numerical computations. It does not require small parameters in algebraic or differential equations as done in the other traditional perturbation methods (regular and singular perturbation). It provides excellent approximations to the solution of non-linear equation with high accuracy.

To the best of the authors’ knowledge, the analysis of heat transfer in convective-radiative porous fin with temperature-dependent internal heat generation and subjected to magnetic field using homotopy perturbation method has not been carried out. Therefore, in this present study, the thermal behavior of convective-radiative porous fin with temperature-dependent internal heat generation and subjected to magnetic field is studied using the homotopy perturbation method. The developed symbolic thermal model is used to investigate the effects of convective, radiative, and magnetic parameters on the thermal performance of the porous fin.

2. PROBLEM FORMULATION

Consider a straight porous fin of length L and thickness t exposed on both faces to a convective environment at temperature T_∞ . The fin is heated internally and subjected to a uniform magnetic field as shown in Figure 1. Assuming the porous medium is homogeneous, isotropic and saturated with a single phase fluid. The physical properties of solid as well as fluid are considered as constant except density variation of liquid, which may affect the buoyancy term where Boussinesq approximation is employed. Fluid and porous media are locally in thermodynamic equilibrium in the domain and surface radiative transfers and non-Darcian effects are negligible, the temperature inside the fin varies along the length only and remains constant with time, there is no thermal contact resistance at the fin base and the fin tip is adiabatic type.

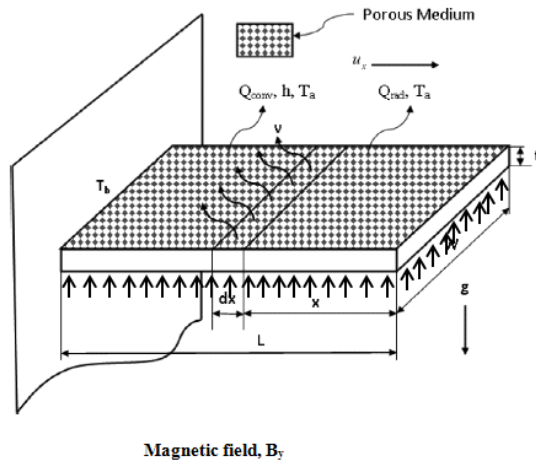


Figure 1. Schematic of the convective-radiative longitudinal porous fin with magnetic field

Based on Darcy's model and following the above assumptions, the thermal energy balance in the fin could be expressed

$$q_x - \left(q_x + \frac{\delta q}{\delta x} dx \right) + q(T) dx = \dot{m} c_p (T - T_a) + hP(1 - \tilde{\varepsilon})(T - T_a) dx + \sigma \varepsilon P(T^4 - T_a^4) dx + \frac{\mathbf{J}_c \times \mathbf{J}_c}{\sigma} dx, \quad (1)$$

where

$$\mathbf{J}_c = \sigma_e (\mathbf{E} + \mathbf{V} \times \mathbf{B}). \quad (2)$$

The mass flow rate of the fluid passing through the porous material can be written as

$$\dot{m} = \rho u(x) W dx. \quad (3)$$

From Darcy's model

$$u(x) = \frac{gK\beta}{v} (T - T_a). \quad (4)$$

Therefore, equation (1) becomes

$$q_x - \left(q_x + \frac{\delta q}{\delta x} dx \right) + q(T) dx = \frac{\rho c_p g K \beta}{v} (T - T_a)^2 dx + hP(1 - \tilde{\varepsilon})(T - T_a) dx + \sigma \varepsilon P(T^4 - T_a^4) dx + \frac{\mathbf{J}_c \times \mathbf{J}_c}{\sigma} dx. \quad (5)$$

As $dx \rightarrow 0$, equation (5) reduces

$$-\frac{dq}{dx} + q(T) = \frac{\rho c_p g K \beta}{v} (T - T_a)^2 + hP(1 - \tilde{\varepsilon})(T - T_a) + \sigma \varepsilon P(T^4 - T_a^4) + \frac{\mathbf{J}_c \times \mathbf{J}_c}{\sigma}. \quad (6)$$

From Fourier's law of heat conduction, the rate of heat conduction in the fin is given by

$$q = -k_{\text{eff}}A_{cr} \frac{dT}{dx} \tag{7}$$

where

$$k_{\text{eff}} = \phi k_f + (1 - \phi)k_s. \tag{8}$$

Following Rosseland diffusion approximation, the radiation heat transfer rate is

$$q = -\frac{4\sigma A_{cr}}{3\beta_R} \frac{dT^4}{dx}. \tag{9}$$

Substituting equation (9) into equation (6) we have

$$\begin{aligned} \frac{d}{dx} \left(k_{\text{eff}}A_{cr} \frac{dT}{dx} + \frac{4\sigma A_{cr}}{3\beta_R} \frac{dT^4}{dx} \right) + q(T) &= \frac{\rho c_p g K \beta}{v} (T - T_a)^2 + \\ &+ hP(1 - \tilde{\varepsilon})(T - T_a) + \sigma \varepsilon P(T^4 - T_a^4) + \frac{\mathbf{J}_c \times \mathbf{J}_c}{\sigma}. \end{aligned} \tag{10}$$

Further simplification of (10) gives the governing differential equation for the fin as

$$\begin{aligned} \frac{d^2T}{dx^2} + \frac{4\sigma}{3\beta_R k_{\text{eff}}} \frac{d}{dx} \left(\frac{dT^4}{dx} \right) - \frac{\rho c_p g K \beta}{k_{\text{eff}} t v} (T - T_a)^2 - \frac{h(1 - \tilde{\varepsilon})}{k_{\text{eff}} t} (T - T_a) - \\ - \frac{\sigma \varepsilon}{k_{\text{eff}} t} (T^4 - T_a^4) - \frac{\mathbf{J}_c \times \mathbf{J}_c}{\sigma k_{\text{eff}} A_{cr}} + \frac{q(T)}{k_{\text{eff}} A_{cr}} = 0. \end{aligned} \tag{11}$$

The boundary conditions are

$$\begin{aligned} x = 0, \quad \frac{dT}{dx} &= 0, \\ x = L, \quad T &= T_b. \end{aligned} \tag{12}$$

But

$$\frac{\mathbf{J}_c \times \mathbf{J}_c}{\sigma} = \sigma B_o^2 u^2. \tag{13}$$

After substitution of equation (13) into equation (11),

$$\begin{aligned} \frac{d^2T}{dx^2} + \frac{4\sigma}{3\beta_R k_{\text{eff}}} \frac{d}{dx} \left(\frac{dT^4}{dx} \right) - \frac{\rho c_p g K \beta}{k_{\text{eff}} t v} (T - T_a)^2 - \frac{h(1 - \tilde{\varepsilon})}{k_{\text{eff}} t} (T - T_a) - \\ - \sigma \varepsilon P(T^4 - T_a^4) - \frac{\sigma B_o^2 u^2}{k_{\text{eff}} A_{cr}} (T - T_a) + \frac{q(T)}{k_{\text{eff}} A_{cr}} = 0. \end{aligned} \tag{14}$$

The case considered in this work is a situation where small temperature difference exists within the material during the heat flow. This actually necessitated the use of temperature-invariant physical and thermal properties of the fin. Also, it has been established that under such scenario, the term T^4 can be expressed as a linear function of temperature. Therefore, we have

$$T^4 = T_\infty^4 + 4T_\infty^3 (T - T_\infty) + 6T_\infty^2 (T - T_\infty)^2 + \dots \cong 4T_\infty^3 T - 3T_\infty^4. \tag{15}$$

Also, it is given that

$$q(T) = q_0 [1 + \lambda (T - T_\infty)].$$

On substituting equation (15) into equation (14), we arrive at

$$\frac{d^2T}{dx^2} + \frac{16\sigma}{3\beta_R k_{\text{eff}}} \frac{d^2T}{dx^2} - \frac{\rho c_p g K \beta}{k_{\text{eff}} t v} (T - T_a)^2 - \frac{h(1 - \tilde{\varepsilon})}{k_{\text{eff}} t} (T - T_a) - 4\sigma \varepsilon P T_a^3 (T - T_a) - \frac{\sigma B_o^2 u^2}{k_{\text{eff}}} A_{cr} (T - T_a) + \frac{q_o}{k_{\text{eff}}} A_{cr} [1 + \lambda(T - T_\infty)] = 0, \quad (16)$$

On introducing the following dimensionless parameters in equation (17) into equation (16),

$$\begin{aligned} X &= \frac{x}{L}, & \theta &= \frac{T - T_a}{T_b - T_a}, & Ra &= \frac{gk\beta(T_b - T_\infty)b}{\alpha\nu k_r}, \\ Nc^2 &= \frac{pb^2h}{k_{\text{eff}}t}, & Rd &= \frac{4\sigma_{st}T_\infty^3}{3\beta_R k_{\text{eff}}}, & Nr &= \frac{4\sigma_{st}bT_\infty^3}{k_{\text{eff}}}, \\ H &= \frac{\sigma B_o^2 u^2}{k_{\text{eff}} A_b}, & Q &= \frac{q_o t}{A_{cr} h (T_b - T_a)} \end{aligned} \quad (17)$$

we arrive at the dimensionless form of the governing equation (16) as

$$(1 + 4Rd) \frac{d^2\theta}{dX^2} - Ra\theta^2 - Nc(1 - \tilde{\varepsilon})\theta - Nr\theta - H\theta + Nc^2Q(1 + \gamma\theta) = 0, \quad (18)$$

or

$$\frac{d^2\theta}{dX^2} - \frac{Ra}{1 + 4Rd}\theta^2 - \frac{Nc(1 - \tilde{\varepsilon})}{1 + 4Rd}\theta - \frac{Nr}{1 + 4Rd}\theta - \frac{H}{1 + 4Rd}\theta + \frac{Nc^2Q}{1 + 4Rd}(1 + \gamma\theta) = 0, \quad (19)$$

Equation (19) can be rewritten as

$$\frac{d^2\theta}{dX^2} - S_h\theta^2 - M_a^2\theta + M^2G(1 + \gamma\theta) = 0, \quad (20a)$$

where

$$\begin{aligned} S_h &= \frac{Ra}{(1 + 4Rd)}, & M^2 &= Nc^2, & G &= \frac{Q}{1 + 4Rd}, \\ M_a^2 &= \frac{Nc(1 - \tilde{\varepsilon})}{1 + 4Rd} + \frac{Nr}{1 + 4Rd} + \frac{H}{1 + 4Rd}. \end{aligned} \quad (20b)$$

The dimensionless boundary conditions are as follows:

$$\begin{aligned} X = 0, & & \frac{d\theta}{dX} &= 0 \\ X = 1, & & \theta &= 1 \end{aligned} \quad (20c)$$

3. METHOD OF SOLUTION BY HOMOTOPY PERTURBATION METHOD

3.1. Choice of a solution method. It is very difficult to develop a closed-form solution for the above non-linear equation (19). Therefore, recourse has to be made to either an approximation analytical method, semi-numerical method or numerical method of solution. In this work, homotopy perturbation method is used to solve the equation.

3.2. The basic idea of the homotopy perturbation method. In order to establish the basic idea behind homotopy perturbation method, consider a system of nonlinear differential equations given as

$$A(U) - f(r) = 0, \quad r \in \Omega \tag{21}$$

with the boundary conditions

$$B\left(u, \frac{\partial u}{\partial \eta}\right) = 0, \quad r \in \Gamma \tag{22}$$

where A is a general differential operator, B is a boundary operator, $f(r)$ is a known analytical function and Γ is the boundary of the domain Ω .

The operator A can be divided into two parts, which are L and N , where L is a linear operator and N is a non-linear operator. Equation (21) can, therefore, be rewritten as follows:

$$L(u) + N(u) - f(r) = 0. \tag{23}$$

By the homotopy technique, a homotopy $U(r, p) : \Omega \times [0, 1] \rightarrow R$ can be constructed, which satisfies the equation

$$H(U, p) = (1 - p)[L(U) - L(U_o)] + p[A(U) - f(r)] = 0, \quad p \in [0, 1] \tag{24}$$

or

$$H(U, p) = L(U) - L(U_o) + pL(U_o) + p[N(U) - f(r)] = 0. \tag{25}$$

In equations (24) and (25) $p \in [0, 1]$ is an embedding parameter, u_o is an initial approximation for equation (19), which satisfies the boundary conditions

Also, from equations (24) and (25) we will have

$$H(U, 0) = L(U) - L(U_o) = 0, \tag{26}$$

$$H(U, 0) = A(U) - f(r) = 0. \tag{27}$$

The changing process of p from zero to unity is just that of $U(r, p)$ from $u_o(r)$ to $u(r)$. This is referred to homotopy in topology. Using the embedding parameter p as a small parameter, the solution of equations (24) and (25) can be assumed to be written as a power series in p as given in (28):

$$U = U_o + pU_1 + p^2U_2 + \dots \tag{28}$$

It should be pointed out that of all the values of p between 0 and $p = 1$ produces the best result. Therefore, setting $p = 1$, results in the approximation solution of equation (21):

$$u = \lim_{p \rightarrow 1} U = U_o + U_1 + U_2 + \dots \tag{29}$$

The basic idea expressed above is a combination of homotopy and perturbation method. Hence, the method is called homotopy perturbation method (HPM), which has eliminated the limitations of the traditional perturbation methods. On the other hand, this technique can have the full advantages of the traditional perturbation techniques. The series (29) is convergent for most cases.

3.3. Application of the homotopy perturbation method to the present problem. According to the homotopy perturbation method (HPM), one can construct an homotopy for equation (19) as

$$H(\theta, p) = (1-p) \left[\frac{d^2\theta}{dX^2} \right] + p \left[\frac{d^2\theta}{dX^2} - S_h\theta^2 - M_a^2\theta + M^2G(1 + \gamma\theta) \right] \quad (30)$$

where $p \in [0, 1]$ is an embedding parameter. For $p = 0$ and $p = 1$ we have

$$\theta(X, 0) = \theta_0(X), \quad \theta(X, 1) = \theta_0(X) \quad (31)$$

We shall assume that the solution of equation (19) can be given in a series of the form

$$\theta(X) = \theta_0(X) + p\theta_1(X) + p^2\theta_2(X) + p^3\theta_2(X) + \dots = \sum_{i=0}^n p^i\theta_i(X). \quad (32)$$

On substituting equation (32) and into equation (30) and expanding the equation and collecting all terms with the same order of together, the resulting equation appears in form of polynomial in p . On equating each coefficient of the resulting polynomial in p to zero, we arrive at a set of differential equations and the corresponding boundary conditions as

$$p^0 : \frac{d^2\theta_0}{dX^2}(X) = 0, \quad \theta_0(0) = 1, \quad \theta'_0(1) = 0; \quad (33)$$

$$p^1 : \frac{d^2\theta_1}{dX^2} + M^2G\gamma\theta_0 - S_h\theta_0^2 - M_a^2\theta_0 + M^2G = 0, \quad \theta_1(0) = 0, \quad \theta'_1(1) = 0; \quad (34)$$

$$p^2 : \frac{d^2\theta_2}{dX^2} + M^2G\gamma\theta_1 - S_h\theta_0\theta_1 - M_a^2\theta_1 = 0, \quad \theta_2(0) = 0, \quad \theta'_2(1) = 0; \quad (35)$$

$$p^3 : \frac{d^2\theta_3}{dX^2} + M^2G\gamma\theta_2 - S_h\theta_1^2 - 2S_h\theta_0\theta_2 - M_a^2\theta_1 + M^2G = 0, \\ \theta_3(0) = 0, \quad \theta'_3(1) = 0; \quad (36)$$

$$p^4 : \frac{d^2\theta_4}{dX^2} - M_a^2\theta_3 - 2S_h\theta_1\theta_2 - 2S_h\theta_0\theta_3 + M^2G\gamma\theta_3 = 0, \\ \theta_4(0) = 0, \quad \theta'_4(1) = 0; \quad (37)$$

$$p^5 : \frac{d^2\theta_5}{dX^2} - S_h\theta_1\theta_3 + M^2G\gamma\theta_4 - M_a^2\theta_4 - S_h\theta_2^2 - 2S_h\theta_0\theta_4 = 0, \\ \theta_5(0) = 0, \quad \theta'_5(1) = 0; \quad (38)$$

$$p^6 : \frac{d^2\theta_6}{dX^2} + M^2G\gamma\theta_5 - 2S_h\theta_0\theta_5 - 2S_h\theta_1\theta_4 - M_a^2\theta_5 - 2S_h\theta_2\theta_3 = 0, \\ \theta_6(0) = 0, \quad \theta'_6(1) = 0; \quad (39)$$

$$p^7 : \frac{d^2\theta_7}{dX^2} + M^2G\gamma\theta_6 - 2S_h\theta_1\theta_5 - 2S_h\theta_0\theta_6 - M_a^2\theta_6 - 2S_h\theta_2\theta_4 = 0, \\ \theta_7(0) = 0, \quad \theta'_7(1) = 0; \quad (40)$$

$$p^8 : \frac{d^2\theta_8}{dX^2} + M^2G\gamma\theta_7 - 2S_h\theta_3\theta_4 - 2S_h\theta_1\theta_6 - M_a^2\theta_7 - 2S_h\theta_0\theta_7 - 2S_h\theta_2\theta_5 = 0, \\ \theta_8(0) = 0, \quad \theta'_8(1) = 0; \quad (41)$$

$$p^9 : \frac{d^2\theta_9}{dX^2} - 2S_h\theta_0\theta_8 - 2S_h\theta_2\theta_6 + M^2G\gamma\theta_8 - S_h\theta_4^2 - 2S_h\theta_3\theta_5 - 2S_h\theta_1\theta_7 - M_a^2\theta_8 = 0, \quad \theta_9(0) = 0, \quad \theta_9'(1) = 0. \quad (42)$$

On solving the above equations (33)-(42) we arrive at

$$\theta_0(X) = 1, \quad (43)$$

$$\theta_1(X) = \frac{1}{2} [M_a^2 - M^2G(1 + \gamma) + S_h] (X^2 - 1), \quad (44)$$

$$\theta_2(X) = \frac{1}{24} [M_a^2 - M^2G(1 + \gamma) + S_h] (M_a^2 + 2S_h - M^2G\gamma) (X^4 - 6X^2 + 5), \quad (45)$$

$$\begin{aligned} \theta_3(X) = & \left\{ \frac{S_h}{4} [M_a^2 - M^2G(1 + \gamma) + S_h]^2 + \right. \\ & \left. + \frac{1}{24} [M_a^2 - M^2G(1 + \gamma) + S_h] (M_a^2 + 2S_h - M^2G\gamma)^2 \right\} \frac{X^6}{30} - \\ & - \left\{ \frac{S_h}{2} [M_a^2 - M^2G(1 + \gamma) + S_h]^2 + \right. \\ & \left. + \frac{1}{4} [M_a^2 - M^2G(1 + \gamma) + S_h] (M_a^2 + 2S_h - M^2G\gamma)^2 \right\} \frac{X^4}{12} + \\ & + \left\{ \frac{S_h}{4} [M_a^2 - M^2G(1 + \gamma) + S_h]^2 + \right. \\ & \left. + \frac{5}{24} [M_a^2 - M^2G(1 + \gamma) + S_h] (M_a^2 + 2S_h - M^2G\gamma)^2 \right\} \frac{X^2}{2} - \\ & - \frac{11S_h}{120} [M_a^2 - M^2G(1 + \gamma) + S_h]^2 + \\ & + \frac{61}{720} [M_a^2 - M^2G(1 + \gamma) + S_h] (M_a^2 + 2S_h - M^2G\gamma)^2. \quad (46) \end{aligned}$$

In the same manner expressions can be obtained for $\theta_4(X)$, $\theta_5(X)$, $\theta_6(X)$, $\theta_7(X)$, $\theta_8(X)$, $\theta_9(X)$. However they are too large expressions to be included in this paper.

From the definition, the solution of equation (19) in HPM domain is

$$\theta(X) = \theta_0(X) + p\theta_1(X) + p^2\theta_2(X) + p^3\theta_3(X) + p^4\theta_4(X) + p^5\theta_5(X) + p^6\theta_6(X) + p^7\theta_7(X) + p^8\theta_8(X) + p^9\theta_9(X) + \dots \quad (47)$$

It should be pointed out that of all the values of p between 0 and 1, $p = 1$ produces the best result. Therefore, setting $p = 1$ results in the approximation solution of equation (19):

$$\begin{aligned} \theta(X) = \lim_{p \rightarrow 1} \theta(X) = & \theta_0(X) + \theta_1(X) + \theta_2(X) + \theta_3(X) + \theta_4(X) + \theta_5(X) + \\ & + \theta_6(X) + \theta_7(X) + \theta_8(X) + \theta_9(X) + \dots \quad (48) \end{aligned}$$

After substituting equations (43)-(47) we have

$$\begin{aligned}
\theta(X) = & 1 - \frac{1}{2} [M_a^2 - M^2G(1 + \gamma) + S_h] (X^2 - 1) + \\
& + \frac{1}{24} [M_a^2 - M^2G(1 + \gamma) + S_h] (M_a^2 + 2S_h - M^2G\gamma) (X^4 - 6X^2 + 5) + \\
& + \left\{ \frac{S_h}{4} [M_a^2 - M^2G(1 + \gamma) + S_h]^2 + \right. \\
& + \left. \frac{1}{24} [M_a^2 - M^2G(1 + \gamma) + S_h] (M_a^2 + 2S_h - M^2G\gamma)^2 \right\} \frac{X^6}{30} - \\
& - \left\{ \frac{S_h}{2} [M_a^2 - M^2G(1 + \gamma) + S_h]^2 + \right. \\
& + \left. \frac{1}{4} [M_a^2 - M^2G(1 + \gamma) + S_h] (M_a^2 + 2S_h - M^2G\gamma)^2 \right\} \frac{X^4}{12} + \\
& + \left\{ \frac{S_h}{4} [M_a^2 - M^2G(1 + \gamma) + S_h]^2 + \right. \\
& + \left. \frac{5}{24} [M_a^2 - M^2G(1 + \gamma) + S_h] (M_a^2 + 2S_h - M^2G\gamma)^2 \right\} \frac{X^2}{2} - \\
& - \frac{11S_h}{120} [M_a^2 - M^2G(1 + \gamma) + S_h]^2 + \\
& + \frac{61}{720} [M_a^2 - M^2G(1 + \gamma) + S_h] (M_a^2 + 2S_h - M^2G\gamma)^2 .
\end{aligned}$$

As regards the parameters S_h , M_a , M and G the reader is referred to equations (20b).

4. RESULTS AND DISCUSSION

Figure 2 shows the effects of porous parameter or porosity on the temperature distribution in the porous fin. From the figures, as the porosity parameter increases, the temperature decreases rapidly and the rate of heat transfer (the convective-radiative heat transfer) through the fin increases as the temperature in the fin drops faster (becomes steeper, reflecting high base heat flow rates) as depicted in the figures. The rapid decrease in fin temperature due to increase in the porosity parameter occurs because as the porosity parameter, Raleigh number increases, the permeability of the porous fin increases and therefore the ability of the working fluid to penetrate through the fin pores increases, the effect of buoyancy force increases and thus the fin convects more heat, the rate of heat transfer from the fin is enhanced and the thermal performance of the fin is increased. Therefore, increase in the porosity of the fin improves fin efficiency by increasing convection heat transfer.

Figure 3 show the effects of conduction-convection parameter on the temperature distribution in the fin. The figure depicts that as the conduction-convection parameter increases, the rate of heat transfer through the fin increases as the temperature in the fin drops faster (becomes steeper, reflecting high base heat flow rates) as depicted

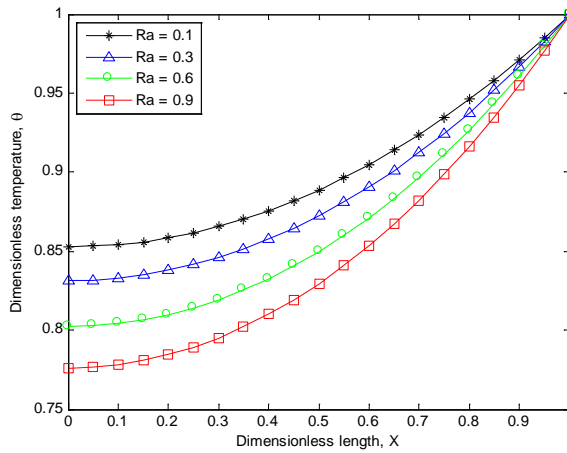


Figure 2. Dimensionless temperature distribution in the fin parameters for varying porous parameter when $Rd = 0.5$, $Nc = 0.6$, $Nr = 0.1$, $\varepsilon = 0.8$ and $Ha = 0.7$, $Q = 0$

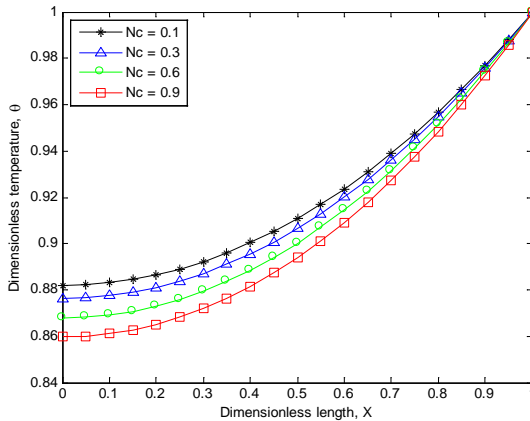


Figure 3. Dimensionless temperature distribution in the fin parameters for varying convection-conduction parameters when $Rd = 0.5$, $Ra = 0.3$, $Nr = 0.2$, $\varepsilon = 0.7$, $Q = 0$ and $Ha = 0.6$

in the figures. The profile has the steepest temperature gradient at lower value of the conduction-convection term, but its much higher value gotten from the lower value of thermal conductivity than the other values of Nc in the profiles produces a lower heat-transfer rate. This shows that the thermal performance or efficiency of the fin is favoured at low values of convective parameter since the aim (high effective use of the fin) is to minimize the temperature decrease along the fin length, where the best

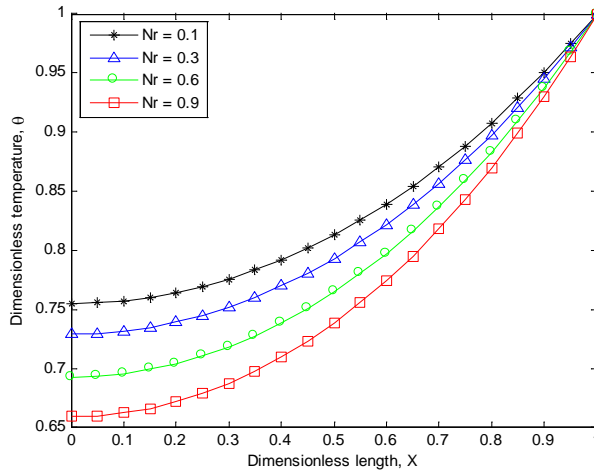


Figure 4. Dimensionless temperature distribution in the fin parameters for varying radiation-conduction parameter when $Rd = 0.8$, $Ra = 0.7$, $Nc = 0.5$, $\varepsilon = 0.2$, $Q = 0$ and $Ha = 0.3$

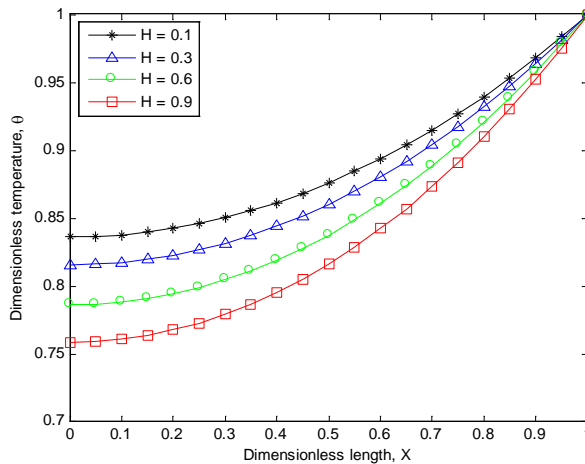


Figure 5. Dimensionless temperature distribution in the fin parameters for varying Hartman number (magnetic parameter), when $Rd = 0.6$, $Ra = 0.5$, $Nc = 0.1$, $Q = 0$, $Nr = 0.7$ and $\varepsilon = 0.4$

possible scenario is when $T = T_b$ everywhere. It must be pointed out that a small value of M corresponds to relatively short and thick fins of poor thermal conductivity and high value of M implies a long fin or fin with low value of thermal conductivity. Since the thermal performance or efficiency of the fin is favoured at low values of convective fin parameter, very long fins are to be avoided in practice.

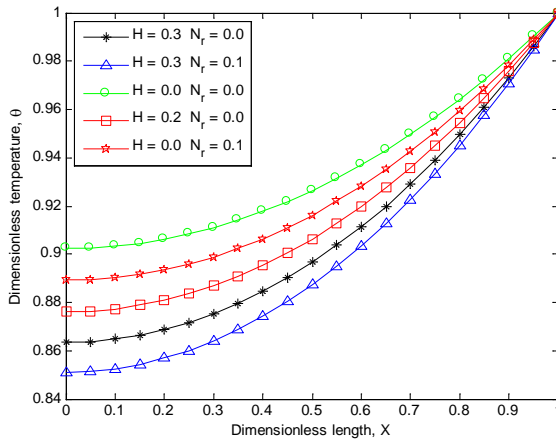


Figure 6. Dimensionless temperature distribution in the fin parameters for varying Hartman parameters and surface-ambient radiation parameters, when $Rd = 0.5$, $Ra = 0.4$, $Nc = 0.3$, $Q = 0$ and $\varepsilon = 0.1$

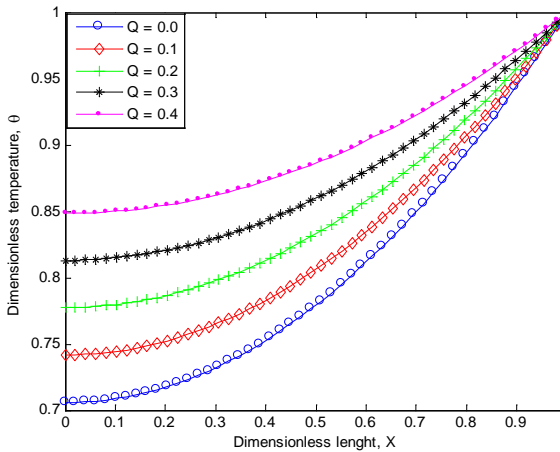


Figure 7. Dimensionless temperature distribution in the fin parameters for varying internal heat generation parameters, when $Rd = 0.25$, $Ra = 2.0$, $Nc = 1.0$, $Nr = 0.8$, $\tilde{a} = 0.2$, $H = 0.4$ and $\varepsilon = 0.2$

The effects of conduction-radiation parameter are shown in Figure 4. The figure shows that with increase in the conduction-radiation parameter, the rate of heat transfer through the fin increases.

Figure 5 shows effects of the magnetic parameter, Hartman number on the temperature distribution in the porous fin. The figure depicts that the induced magnetic field in the fin can improve heat transfer through porous fins. This is also depicted in Figure 6 and it is also shown that conduction-radiation parameter increases the thermal performance of the fin.

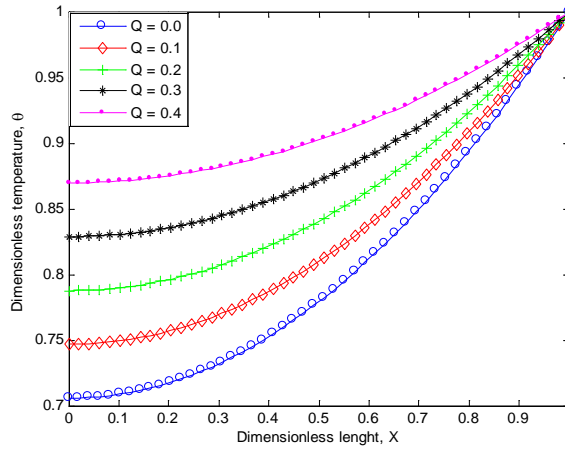


Figure 8. Dimensionless temperature distribution in the fin parameters for varying internal heat generation parameters, when $Rd = 0.25$, $Ra = 2.0$, $Nc = 1.0$, $Nr = 0.8$, $\tilde{a} = 0.4$, $H = 0.4$ and $\varepsilon = 0.2$

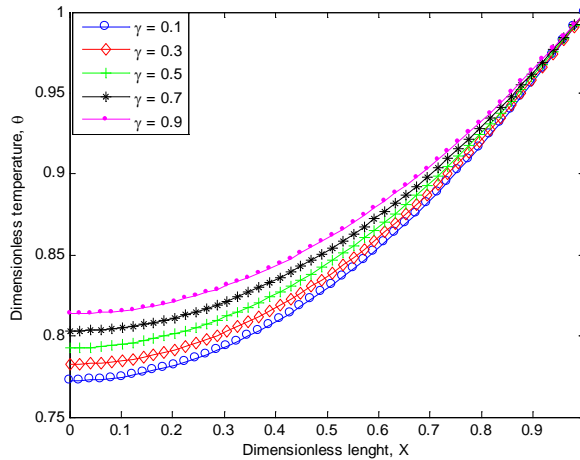


Figure 9. Dimensionless temperature distribution in the fin parameters for varying temperature-dependent internal heat generation parameters, when $Rd = 0.25$, $Ra = 2.0$, $Nr = 0.8$, $Nc = 1.0$, $H = 0.4$, $Q = 0.2$ and $\varepsilon = 0.2$

From Figure 2-6 it is shown that increase in porosity, convective, radiative and magnetic parameters increases the rate of heat transfer from the fin and consequently improves the efficiency of the fin.

Figures 7 and 8 show the effects of internal heat generation parameter on the temperature distribution in the porous fin while Figures 9 and 10 depict the effects of

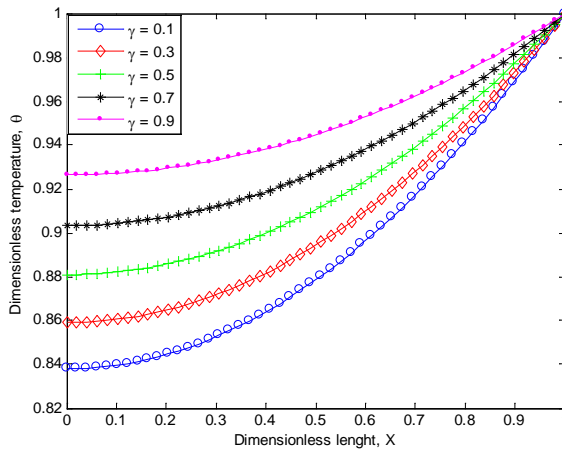


Figure 10. Dimensionless temperature distribution in the fin parameters for varying temperature-dependent internal heat generation parameters, when $Rd = 0.25$, $Ra = 2.0$, $Nr = 0.8$, $Nc = 1.0$, $H = 0.4$, $Q = 0.4$ and $\varepsilon = 0.2$

Table 1. Comparison of results of NM and HPM for $\theta(X)$ and $Rd = 0.5$, $\varepsilon = 0.1$, $Ra = 0.4$, $Nc = 0.3$, $Q = 0$, $Nr = 0.2$, $H = 0.1$

X	NM	HPM	Absolut Error
0.00	0.863499231	0.863499664	0.000000433
0.05	0.863828568	0.863829046	0.000000478
0.10	0.864817090	0.864817539	0.000000449
0.15	0.866466182	0.866465743	0.000000439
0.20	0.868776709	0.868776261	0.000000448
0.25	0.871751555	0.871751104	0.000000451
0.30	0.875393859	0.875393404	0.000000455
0.35	0.879707472	0.879707010	0.000000462
0.40	0.884696967	0.884696500	0.000000467
0.45	0.890367650	0.890367181	0.000000469
0.50	0.896725569	0.896725096	0.000000473
0.55	0.903777531	0.903777060	0.000000471
0.60	0.911531120	0.911530658	0.000000462
0.65	0.919994710	0.919994259	0.000000451
0.70	0.929177488	0.929177056	0.000000432
0.75	0.939089476	0.939089079	0.000000397
0.80	0.949741555	0.949741203	0.000000352
0.85	0.961145491	0.961145189	0.000000302
0.90	0.973313964	0.973313764	0.000000200
0.95	0.986260599	0.986260549	0.000000005
1.00	1.000000000	1.000000000	0.000000000

temperature-dependent internal heat generation parameter on the temperature distribution in the fin. From the figures, as the internal heat generation parameters increase the temperature gradient of the fins decreases and consequently, the rate of heat transfer in the fin decreases. It should be stated that fins with porous material give superior performance with a significant reduction in weight compared with solid metal fins because of low thermal conductivity and the large area of the material that comes in contact with the cooling fluid.

Table 1 shows a comparison of results and the errors in the method used in this study. It could be inferred from the table that the HPM is highly accurate and agrees very well with the numerical method.

5. CONCLUSION

In this work, thermal performance in a porous fin temperature-dependent thermal properties and internal heat generation has been analyzed using the homotopy perturbation method. The developed symbolic heat transfer models were used to investigate the effects of various parameters on the thermal performance of the porous fin. Increasing the porosity increases the rate of heat transfer from the base of the fin and consequently improve the efficiency of the fin. Also, decreasing thermal conductivity parameter, results in increase in the rate of heat transfer from the base of the fin. The homotopy perturbation method used in the work was validated with the numerical method using Runge-Kutta method. The homotopy perturbation method results are in excellent agreement with results of the numerical method.

6. NOMENCLATURE

Latin symbols

A_{cr}	cross sectional area of porous fin surface area, m^2 ,
B	magnetic induction (T),
B_o	magnetic field intensity (T),
c_p	specific heat capacity, $J/(kgK)$,
Da	Darcy number,
E	electric field, V/m ,
g	acceleration due to gravity, m/s^2 ,
h	heat transfer coefficient, $Wm^{-2}k^{-1}$,
h_b	heat transfer coefficient at the base of the fin, $Wm^{-2}k^{-1}$,
J_c	conduction current intensity (A),
k	thermal conductivity of the fin material, $Wm^{-1}k^{-1}$,
k_b	thermal conductivity of the fin material at the base of the fin, $Wm^{-1}k^{-1}$,
k_{eff}	effective thermal conductivity, $Wm^{-1}k^{-1}$,
K	permeability of the porous fin, m^2 ,
L	length of the fin, m ,
M	dimensionless thermo-geometric parameter,
m	mass flow rate of fluid passing through porous fin, kg/s ,
Nu	Nusselt number,

Nc	convective heat parameter,
Nr	radiative heat parameter,
P	perimeter of the fin, m ,
q	internal heat generation, W/m^3 ,
Q	dimensionless heat transfer rate per unit area,
q_b	heat transfer rate per unit area at the base, W/m^2
Q_b	dimensionless heat transfer rate at the base of porous fin,
Q_s	dimensionless heat transfer rate the base in solid fin,
R_d	Radiation-conduction parameter,
Ra	Rayleigh number,
S_h	porosity parameter,
t	thickness of the fin, m ,
T	fin temperature, K ,
T_a	ambient temperature, K ,
T_b	fin base temperature, K ,
v	average velocity of fluid passing through porous fin, m/s ,
V	particle's velocity, m/s ,
x	axial length measured from fin tip, m ,
X	dimensionless length of the fin,
W	width of the fin, m .

Greek symbols

β	thermal conductivity parameter or non-linear parameter,
β'	coefficient of thermal expansion (K^{-1}),
$\tilde{\varepsilon}$	pores parameter ,
ϕ	porosity or void ratio,
δ	fin thickness at its base, m ,
δ_b	fin thickness at its base, m ,
λ	dimensional internal heat generation parameter,
γ	dimensionless internal heat generation parameter,
θ	dimensionless temperature,
θ_b	dimensionless temperature at the base of the fin,
η	efficiency of the fin,
ν	kinematic viscosity, m^2/s ,
ρ	density of the fluid, kg/m^3 ,
σ	Stefan-Boltzmann constant,
σ_e	particle charge, C .

REFERENCES

1. KIWAN, S. and AL-NIMR, A.: Using porous fins for heat transfer enhancement. *ASME Journal of Heat Transfer*, **123**, (2001), 790–795.
2. KIWAN, S.: Effect of radiative losses on the heat transfer from porous fins. *International Journal of Thermal Sciences*, **46**, (2007), 1046-1055
3. KIWAN, S.: Thermal analysis of natural convection porous fins. *Transport in Porous Media*, **67**, (2007), 17-29.

4. KIWAN, S. and ZEITOUN, O.: Natural convection in a horizontal cylindrical annulus using porous fins. *International Journal of Heat and Fluid Flow*, **18**(5), (2008), 618-634.
5. GORLA, R. S. and BAKIER, A. Y.: Thermal analysis of natural convection and radiation in porous fins. *International Communications in Heat and Mass Transfer*, **38**, (2011), 638-645.
6. KUNDU, B. and BHANJI, F.: An analytical prediction for performance and optimum design analysis of porous fins. *International Journal of Refrigeration*, **34**, (2011), 337-352.
7. KUNDU, B., BHANJI, F. and LEE, K. S.: A model on the basis of analytics for computing maximum heat transfer in porous fins. *International Journal of Heat and Mass Transfer*, **55**(25-26), (2012), 7611-7622.
8. TAKLIFI, A., AGHANAJAFI, C. and AKRAMI, H.: The effect of MHD on a porous fin attached to a vertical isothermal surface. *Transport in Porous Media*, **85**, (2010), 215-31.
9. BHANJA, D. and KUNDU, B.: Thermal analysis of a constructal T-shaped porous fin with radiation effects. *International Journal of Refrigeration*, **34**, (2011), 1483-1496.
10. KUNDU B.: Performance and optimization analysis of SRC profile fins subject to simultaneous heat and mass transfer. *International Journal of Heat and Mass Transfer*, **50**, (2007), 1545-1558.
11. GORLA, R., DARVISHI, R. S. and KHANI, M. T.: Effects of variable thermal conductivity on natural convection and radiation in porous fins. *International Communications in Heat and Mass Transfer*, **38**, (2013), 638-645.
12. SAEDODIN, S. and SHAHBABAEI, M.: Thermal analysis of natural convection in porous fins with homotopy perturbation method (HPM). *Arabian Journal for Science and Engineering*, **38**, (2013), 2227-2231.
13. DARVISHI, M. T., GORLA, R. S. R., GORLA, R. and AZIZ, A.: Thermal performance of a porous radial fin with natural convection and radiative heat losses. *Thermal Science*, **19**(2), (2015), 669-678.
14. MORADI, A., HAYAT, T. and ALSAEDI, A.: Convective-radiative thermal analysis of triangular fins with temperature-dependent thermal conductivity by DTM. *Energy Conversion and Management*, **77**, (2014), 70-77.
15. HA, H. GANJI, D. D. and ABBASI, M.: Determination of temperature distribution for porous fin with temperature-dependent heat generation by homotopy analysis method. *Journal of Applied Mechanical Engineering*, **4**(1), (2005), 1-5.
16. HOSHYAR, H. A., RAHIMIPETROUDI, I., GANJI, D. D. and MAJIDIAN, A. R.: Thermal performance of porous fins with temperature-dependent heat generation via homotopy perturbation method and collocation method. *Journal of Applied Mathematics and Computational Mechanics*, **14**(4), (2015), 53-65.
17. HATAMI, D. and GANJI, D. D.: Thermal performance of circular convective-radiative porous fins with different section shapes and materials. *Energy Conversion and Management*, **76**, (2013), 185-193.
18. HATAMI, D. and GANJI, D. D.: Thermal behavior of longitudinal convective-radiative porous fins with different section shapes and ceramic materials (SiC and Si₃N₄). *International of J. Ceramics International*, **40**, (2014), 6765-6775.

19. ROSTAMIYAN, Y., GANJI, D. D., PETROUDI, I. R. and NEJAD, K. M.: Analytical investigation of nonlinear model arising in heat transfer through the porous fin. *Thermal Science*, **18**(2), (2014), 409-417.
20. GHASEMI, S. E., VALIPOUR, P., HATAMI, M. and GANJI D. D.: Heat transfer study on solid and porous convective fins with temperature-dependent heat -generation using efficient analytical method. *Journal of Central South University of Technology*, **21**, (2014), 4592-4598.
21. HE, J. H.: Homotopy perturbation technique. *Computer Methods in Applied Mechanics and Engineering*, **178**, (1999), 257-262.
22. HE, J. H.: New interpretation of homotopy perturbation method. *International Journal of Modern Physics B*, **20**, (2006), 2561-2568.
23. HE, J. H.: A coupling method of homotopy technique and perturbation technique for nonlinear problems. *International Journal of Non-Linear Mechanics*, **35**, (2000), 37-43.
24. HE, J. H.: Some asymptotic methods for strongly nonlinear equations. *International Journal of Modern Physics B*, **20**, (2006), 1141-1199.
25. HE, J. H.: New perturbation technique which is also valid for large parameters. *Journal of Sound and Vibration*, **229**, (2000), 1257-1263.

Notes for Contributors

to the Journal of Computational and Applied Mechanics

Aims and scope. The aim of the journal is to publish research papers on theoretical and applied mechanics. Special emphasis is given to articles on computational mechanics, continuum mechanics (mechanics of solid bodies, fluid mechanics, heat and mass transfer) and dynamics. Review papers on a research field and materials effective for teaching can also be accepted and are published as review papers or classroom notes. Papers devoted to mathematical problems relevant to mechanics will also be considered.

Frequency of the journal. Two issues a year (approximately 80 pages per issue).

Submission of Manuscripts. Submission of a manuscript implies that the paper has not been published, nor is being considered for publication elsewhere. Papers should be written in standard grammatical English. The manuscript is to be submitted in electronic, preferably in pdf, format. The text is to be 130 mm wide and 190 mm long and the main text should be typeset in 10pt CMR fonts. Though the length of a paper is not prescribed, authors are encouraged to write concisely. However, short communications or discussions on papers published in the journal must not be longer than 2 pages. Each manuscript should be provided with an English Abstract of about 50–70 words, reporting concisely on the objective and results of the paper. The Abstract is followed by the Mathematical Subject Classification – in case the author (or authors) give the classification codes – then the keywords (no more than five). References should be grouped at the end of the paper in numerical order of appearance. Author’s name(s) and initials, paper titles, journal name, volume, issue, year and page numbers should be given for all journals referenced.

The journal prefers the submission of manuscripts in L^AT_EX. Authors should prefer the $\mathcal{A}\mathcal{M}\mathcal{S}$ -L^AT_EX article class and are not recommended to define their own L^AT_EX commands. Visit our home page for further details concerning how to edit your paper.

For the purpose of refereeing the manuscripts should be sent either to Balázs Tóth (Balazs.TOTH@uni-miskolc.hu) or György SZEIDL (Gyorgy.SZEIDL@uni-miskolc.hu).

The eventual supply of an accepted for publication paper in its final camera-ready form will ensure more rapid publication. Format requirements are provided by the home page of the journal from which sample L^AT_EX files can be downloaded:

<http://www.mech.uni-miskolc.hu/jcam>

These sample files can also be obtained directly (via e-mail) from Balázs TÓTH (Balazs.TOTH@uni-miskolc.hu), upon request.

One issue of the journal and ten offprints will be provided free of charge and mailed to the correspondent author. Since JCAM is an open access journal each paper can be downloaded freely from the homepage of the journal.

The Journal of Computational and Applied Mechanics is abstracted in Zentralblatt für Mathematik and in the Russian Referativnij Zhurnal.

Secretariat of the Vice-Rector for Research and International Relations, University of Miskolc
Responsible for publication: Prof. Dr. Tamás Kékesi
Published by the Miskolc University Press under the leadership of Attila Szendi
Responsible for duplication: Works manager Erzsébet Pásztor
Number of copies printed: 75
Put to the Press on December 14, 2017
Number of permission: TNRT. 2018-20.ME

HU ISSN 1586–2070

A Short History of the Publications of the University of Miskolc

The University of Miskolc (Hungary) is an important center of research in Central Europe. Its parent university was founded by the Empress Maria Teresia in Selmecebánya (today Banská Štiavnica, Slovakia) in 1735. After the first World War the legal predecessor of the University of Miskolc moved to Sopron (Hungary) where, in 1929, it started the series of university publications with the title *Publications of the Mining and Metallurgical Division of the Hungarian Academy of Mining and Forestry Engineering* (Volumes I.-VI.). From 1934 to 1947 the Institution had the name Faculty of Mining, Metallurgical and Forestry Engineering of the József Nádor University of Technology and Economic Sciences at Sopron. Accordingly, the publications were given the title *Publications of the Mining and Metallurgical Engineering Division* (Volumes VII.-XVI.). For the last volume before 1950 – due to a further change in the name of the Institution – *Technical University, Faculties of Mining, Metallurgical and Forestry Engineering, Publications of the Mining and Metallurgical Divisions* was the title.

For some years after 1950 the Publications were temporarily suspended.

After the foundation of the Mechanical Engineering Faculty in Miskolc in 1949 and the movement of the Sopron Mining and Metallurgical Faculties to Miskolc, the Publications restarted with the general title *Publications of the Technical University of Heavy Industry* in 1955. Four new series - Series A (Mining), Series B (Metallurgy), Series C (Machinery) and Series D (Natural Sciences) - were founded in 1976. These came out both in foreign languages (English, German and Russian) and in Hungarian.

In 1990, right after the foundation of some new faculties, the university was renamed to University of Miskolc. At the same time the structure of the Publications was reorganized so that it could follow the faculty structure. Accordingly three new series were established: Series E (Legal Sciences), Series F (Economic Sciences) and Series G (Humanities and Social Sciences). The latest series, i.e., the series H (European Integration Studies) was founded in 2001. The eight series are formed by some periodicals and such publications which come out with various frequencies.

Papers on computational and applied mechanics were published in the

Publications of the University of Miskolc, Series D, Natural Sciences.

This series was given the name Natural Sciences, Mathematics in 1995. The name change reflects the fact that most of the papers published in the journal are of mathematical nature though papers on mechanics also come out.

The series

Publications of the University of Miskolc, Series C, Fundamental Engineering Sciences

founded in 1995 also published papers on mechanical issues. The present journal, which is published with the support of the Faculty of Mechanical Engineering and Informatics as a member of the Series C (Machinery), is the legal successor of the above journal.



Journal of Computational and Applied Mechanics

Volume 12, Number 2 (2017)

Contents

Contributed Papers

- Károly JÁRMAI and György SZEIDL: Preface 81-83
- Camelia CERBU and Horatiu TEODORESCU-DRAGHICESCU: Aspects on modeling the mechanical behavior of aluminum alloys with different heat treatments 85-98
- Chavi MAHESHWARI, Govind PATHAK and Satya. P. GUPTA: Unsteady MHD free convective heat and mass transfer flow with variable heat and mass fluxes 99-107
- Dávid GÖNCZI: Thermoelastic analysis of thick-walled functionally graded spherical pressure vessels with temperature-dependent material properties 108-125
- Gbeminiyi SOBAMOWO, Olurotimi ADELEYE and Ahmed YINUSA: Analysis of convective-radiative porous fin with temperature-dependent internal heat generation and magnetic field using homotopy perturbation method 127-145